Prospects for open heavy flavor measurements via dimuons in Pb-Pb collisions at $\sqrt{}$ s N N = 5.5 TeV with the ALICE Muon Forward Tracker

Samir Assouabi

Master Sciences de la matière

Deuxième année

Spécialité : Physique des Particules

Rapport de stage

Juin 2015

Laboratoire de Physique Corpusculaire

Université Blaise Pascal

Prospects for open heavy flavor measurements via dimuons in Pb-Pb collisions at $\sqrt{s_{NN}} = 5.5$ TeV with the ALICE Muon Forward Tracker

Samir ASSOUABI

Responsable de stage : Lizardo VALENCIA PALOMO

Acknowledgments

First, I'd like to thank Lizardo for his continuous and tireless efforts, making this intership truely satisfactory. I am glad to have accomplished this task with him, and definitely think that it was fruitful. It has been a little bit more than four months, and I am rejoiced to see the result.

I'd also like to thank the whole laboratory and its personnel, for having provided the conditions to perform this intership in a convenient fashion.

Contents

1 Introduction

The ALICE (A Large Ion Collider Experiment) experiment is one the four main experiments at the LHC (Large Hadron Collider). ALICE was designed to study high energy heavy ion collisions. These collisions fulfill the requirements to recreate a state of matter where quarks and gluons, usually confined inside structures called "hadrons", become deconfined. This state of matter is known as the Quark Gluon Plasma (QGP), and the Universe, one microsecond after the Big Bang, was in a QGP state.

Due to the extremely short life-time of the QGP, a direct observation of the plasma is not possible. Among the possible probes of the QGP, heavy quarks are of particular interest because they are produced in the hard-scattering processes and experience the whole evolution of the system.

As it is the case for many LHC experiments, ALICE will be upgraded over the years. One of the ALICE upgrades scheduled for the run III of the LHC (that will start in 2019) is the Muon Forward Tracker (MFT). The MFT will be used in conjunction with the muon spectrometer at forward rapidities and the upgraded Inner Tracking System detectors, in the central barrel. A current muon spectrometer's setup limitation is the impossibility to distinguish beauty and charm hadrons through their semimuonic decays. The MFT is expected to address this by allowing such distinction.

In order to separate the open charm and open beauty, there exists an observable, called the offset, that can be used. Due to the different mean lifetimes of the beauty and charm hadrons, their offset distributions would be significantly different. Separating the muons coming from open charm and open beauty will give us more insight on the QGP.

In this study, we'll evaluate the future MFT perfomances in Pb-Pb collisions for the open charm and open beauty measurements, using the offset distributions, via dimuons. For this, we'll start by defining the theoretical and experimental frameworks. Then we'll use a Monte-Carlo simulation of Pb-Pb collisions, generated with the expected conditions of run III, to evaluate the uncertainties for the open beauty and open charm extraction with the MFT.

2 Physics motivation

This first part will introduce the physics of this internship, begining by the theoretical background (the Standard Model) with a brief description of its main concepts, followed by a closer look at the physics motivations that are pursued through this study, first by introducing the particles studied (open heavy flavors), and then by explaining the interests in their study.

2.1 Heavy ion collisions and Quark Gluon Plasma (QGP)

2.1.1 The Standard Model

The Standard Model is the theory that describes the elementary particles and their interactions[1]. Among the fundamental particles, there are six quarks (q) that are grouped in three families:

$$\begin{pmatrix} up \\ down \end{pmatrix} \begin{pmatrix} charm \\ strange \end{pmatrix} \begin{pmatrix} top \\ beauty \end{pmatrix}$$

Quark composed particles are called hadrons. Hadrons are in turn divided into two groups: baryons made of three quarks ($qq'q''$), and mesons made of a quark and an antiquark ($q\bar{q'}$). Where q, q', $\bar{q'}$ and q'' are any of the previously mentionned quarks, except the top quark that decays before it can hadronize due to its very large mass (~ 173 GeV/c^2)[2].

The Standard Model describes three fundamental interactions: electromagnetic, weak and strong. For each interaction, there are gauge bosons associated to it that act like "force carriers": the electromagnetic interaction has one gauge boson called the photon (γ); the weak interactions has three massive gauge bosons named W^+, W^- and Z^0; and the strong interaction has eight massless bosons called gluons (g). In addition to that, the Standar Model features another bosonic particle which is not a gauge boson: the Higgs boson. It is responsible for the masses of the other particles.

In this study we'll focus on particles that have either a charm (c) or beauty (b) quark in its composition, called open heavy flavor (D and B hadrons, respectively) because of the significant masses of these two quarks ($\sim$ 1 GeV for the charm and $\sim$ 4 GeV for the beauty).

There are another kind of particles, called leptons: the electron (e), muon (μ) and tau (τ) particles. Each of them have an associated neutrino (ν_e, ν_μ and ν_τ). The present report will focus on muons from the weak decay of open heavy flavors.

2.1.2 Quantum Chromodynamics (QCD)

The Quantum Chromodynamics (QCD) theory, within the Standard Model, is the theory that describes the strong interation, it is how we understand the stability of the atomic nucleus, and it is at the origin of all hadronic structures.

The color is the charge of the strong interaction, pretty much like the electrical charge is the charge of the electromagnetic interaction. There are three colors: red (R), green (G) and blue (B), and three anti-colors: anti-red ($\bar{R}$), anti-green ($\bar{G}$) and anti-blue ($\bar{B}$). Quarks and gluons are color-charged particle, that's why they interact strongly, and also the reason why they can't be isolated. A particle can be isolated only if its color charge is "white" (or "neutral").

2.1.3 The Quark Gluon Plasma

The QCD predicts a state of matter, extrememly hot and dense, in which quarks and gluons are deconfined.

This asymptotic freedom is reached when the coupling constant α_s of the strong interaction drops (asymptotically) to zero. This constant is defined as [3]:

$$\alpha_s(Q^2) = \frac{4\pi}{\beta_0 \ln(Q^2/\Lambda^2_{QCD})}$$

where Q is the transferred momentum, $\beta_0 = 11 - \frac{2}{3}n_f$ with n_f the number of flavors and $\Lambda_{QCD} \approx 200$ MeV is the QCD scale parameter; it is the energy scale where the perturbative approach of the Quantum Chromodynamics (pQCD) cannot be applied anymore.

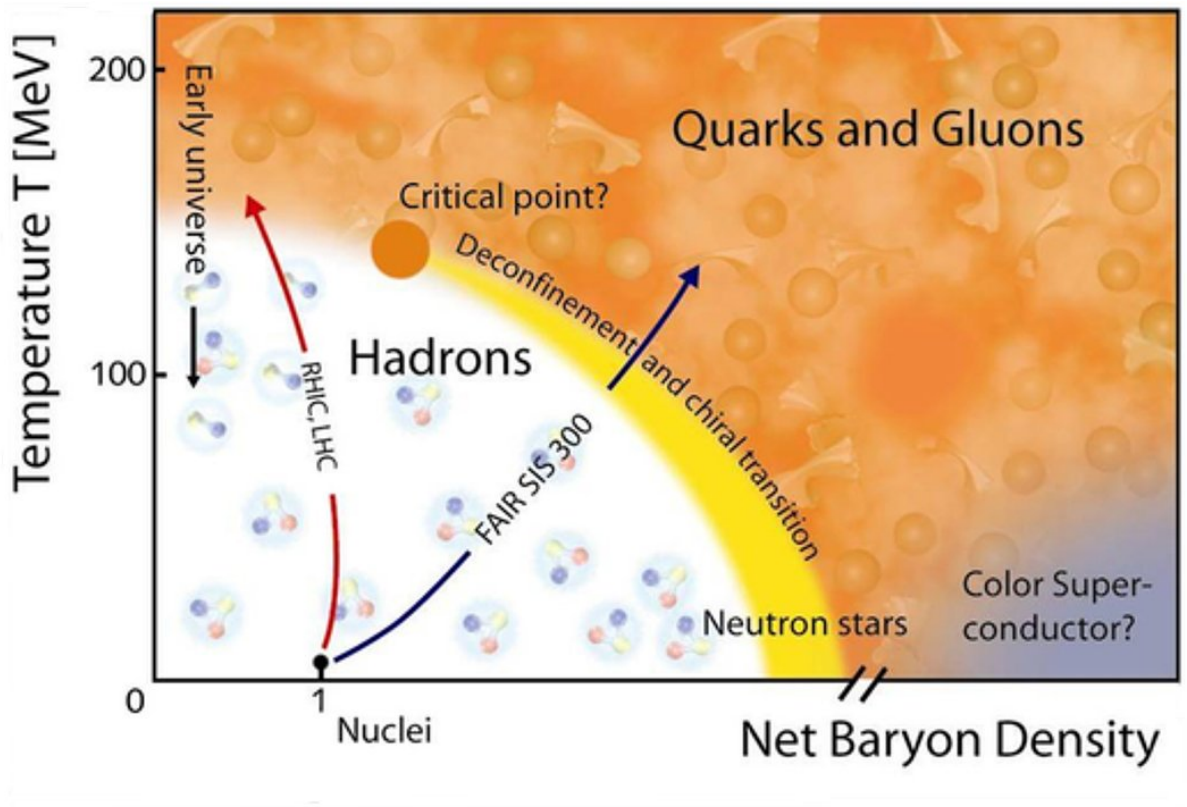

Figure 2.1: The QCD phase space, with hadronic and QGP states. The arrows indicate areas probed by various colliders, including the LHC (for the heavy ion collisions only).

This state of matter created by the deconfinement of quarks and gluons is called Quark Gluon Plasma (QGP). Figure 2.1 shows the QCD phase diagram, and the regions probed by several particle accelerators including the LHC. It shows the state of matter depending on two variables: the temperature and the net baryon density. The net baryon density is the density of baryon minus the density of anti-baryon. The ordinary nuclear matter is in the "hadrons" part of the diagram, in the dot at a net baryon density equal to 1 and low temperature. In this region, quarks are confined and form hadrons. In the orange portion of the diagram indicates the temperature and net baryon density values for which the quarks are deconfined, it is the QGP state. A blue portion, at low temperature and very high net baryon densities, called "Color Super-conductor?" is a possible state of matter that is similar to the already-known (electrical) superconductivity in which electrons form pairs, called Cooper pairs, and behave as bosons. A color-superconductor would happen when quarks become correlated and form pairs also

called Cooper pairs. It is believed that such state of matter would exist inside neutron stars which have very high net baryon densities and at the same time are not too hot[4]. On the QCD phase space, another arrow indicates "early Universe": it is belived that for a very short amount of time (between $t \sim 10^{-11}\ s$ and $t \sim 10^{-4}\ s$ after the Big Bang), the Universe was in a QGP state[5].

The lifetime of the QGP is extrememly short, and cannot be observed directely. Good candidates for its study are, among others, open heavy flavors, as their inetractions with the QGP would give us more insights on it.

2.1.4 Heavy ion collisions

Heavy ion collisions provide the energy (temperature) and baryonic density required to produce, in the laboratory, the QGP.

We can't deduce much from these heavy ion collisions alone, without having a reference, that's why we use proton-proton collisions. Heavy ion collisions don't only produce QGP, as ions are hadronic structures, they also interact through regular nuclear interactions. These interaction, called "cold nuclear matter effects", must be distinguished from the ones due to the QGP ("hot nuclear matter effects"). In order to do so, we perform a third kind of collisions: proton-heavy ion. In these collisions, the heavy ion will interact through cold nuclear interactions, but we don't expect any QGP production, so that way we can evaluate the impact of the cold nuclear interactions, and be able to not confuse them with the ones due to the QGP in the heavy ion collisions.

2.2 Open heavy flavors and their interests in the QGP study

2.2.1 Open Heavy Flavors

Among the Standard Model possible combinations of quarks, we have mesons, which are quark-antiquark combinations. Quarkonia are bound states of heavy quark and heavy anti-quark. When only one of the two quarks is a heavy quark (either charm or beauty quark or anti-quark), we give them the name of "open heavy flavor". The D and B mesons are the main open heavy flavors studied in this analysis, several of their physical properties (quark content, mass, mean lifetime and electrical charge) are avialable in tables 2.1 and 2.2. The production of baryonic open heavy flavor is also taken into account, but it is a very small percentage of the open heavy flavor production in heavy ion collisions.

D meson	Quark composition	Mass	Mean lifetime	Electrical charge
D^-	$\bar{c}d$	1869.62 ± 0.15 MeV/c^2	$(1040 \pm 7) \times 10^{-15}\ s$	-1
D^+	$c\bar{d}$			$+1$
D^0	$c\bar{u}$	1864.86 ± 0.13 MeV/c^2	$(410.1 \pm 1.5) \times 10^{-15}\ s$	0
$\bar{D}^0$	$\bar{c}u$			

Table 2.1: Table of D mesons[2].

B meson	Quark composition	Mass	Mean lifetime	Electrical charge
B^-	$\bar{b}d$	5279.25 ± 0.17 MeV/c^2	$(1.641 \pm 0.0008) \times 10^{-12}\ s$	-1
B^+	$b\bar{d}$			$+1$
B^0	$b\bar{u}$	5279.58 ± 0.17 MeV/c^2	$(1.519 \pm 0.0007) \times 10^{-12}\ s$	0
$\bar{B}^0$	$\bar{b}u$			

Table 2.2: Table of B mesons[2].

The heavy quarks are produced at the very beginning of the collision, during the hard scattering step which takes place around $t < 1$ fm/c (for example, for the $c\bar{c}$ pairs it's 0.08 fm/c)[5], and thus undergo the whole medium evolution. The QGP appears around $t \approx 10 - 15$ fm/c, and hadronization occurs around $t \approx 20$ fm/c, the deconfined state ends and quarks and gluons get confined again[3]. This space-time evolution of a high energy heavy ion collision is graphically represented in figure 2.2.

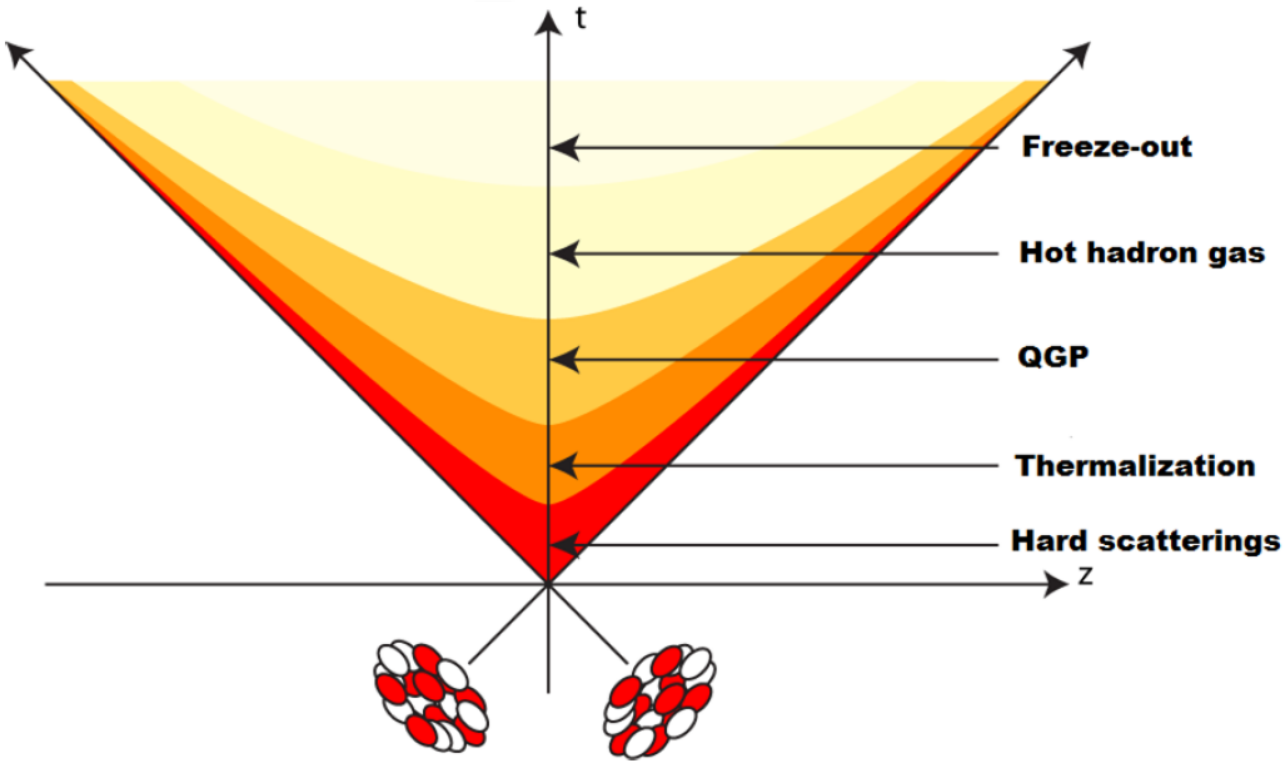

Figure 2.2: Heavy ion collision space-time evolution[5].

2.2.2 Nuclear modification factor

The nuclear modification factor (R_{AA}) compares the production rate of a given particle in heavy-ion collisions with respect to proton-proton times a scaling factor. It is defined as [5]:

$$R_{AA}(p_T) = \frac{1}{< N_{coll} >} \cdot \frac{dN_{AA}/dp_T}{dN_{pp}/dp_T}$$

where $< N_{coll} >$ is the mean number of binary collisions, dN_{AA}/dp_T and dN_{pp}/dp_T are the production yields in ion-ion and proton-proton collisions as functions of the p_T. The nuclear modification can also be computed as a function of the centrality of the collision or the rapidity.

Another QCD predictement is that the energy loss of quarks and gluons through the medium depends on their color-charge. This effect called "in-medium energy loss", which states that gluons should lose more energy inside the deconfined medium than quarks. The "Dead-cone effect implies that there is a mass ordering in the energy loss due to the gluon radiation suppression. This can be experimentally verified by measuring the nuclear modification factors for beauty hadrons, charm hadrons and pions. If it is actually the case then we should have it the end: $R^B_{AA} > R^D_{AA} > R^\pi_{AA}$.

Obtaining the nuclear modification factors for beauty and charm separately and as functions of the p_T would allow us to deduce if the QGP produced is strongly or weakly interacting. If it is weakly interacting, then the pQCD computations give a specific $R^c_{AA}(p_T)/R^b_{AA}(p_T)$ ratio evolution with the p_T.

If not, the prediction from a strongly coupled AdS/CFT energy loss model has a very different ratio evolution with the p_T [5].

2.3 Some useful definitions

We need to define a few high energy physics observables that will be needed in the following chapters.

First, we define the rapidity as: $y = \frac{1}{2}\ln(\frac{E+p_z}{E-p_z})$, where p_z is the particle's momentum component along the beam axis (the z-axis), and E is the energy of the particle.

The pseudorapidity (η) is defined as: $\eta = -\ln(\tan(\theta/2))$ with θ the angle between the beam and the trajectory of the particle.

We quantify the performance of a particle collider using its center-of-mass energy ($\sqrt{s}$) and its luminosity (L). The second is defined as [5]:

$$L = fnN^2/A$$

where f is the revolution frequency, n is the number of bunches in both beams, N is the number of particles per bunch and A is the cross sectional area of the beams. The luminosity has the dimension of the inverse of area times unit of time ($m^{-2}{\cdot}s^{-1}$) in SI units. However, in nuclear and particle physics, the unit of area is oftenly called barn (b).

We also use the integrated luminosity (L_{int}), usually expressed in inverse barns, to quantify the global luminosity of a collider over a given amount of time:

$$L_{int} = \int L \, \mathrm{d}t$$

Finally, the centrality of the collision is expressed in percentage. A low centrality percentage means that the the two heavy ions are colliding almost totally frontally (the overlap between them is almost total), in this case we call it a central collision. On the contrary, a high centrality percentage means that the two heavy ions just brush slightly, and it is named a peripherical collision.

3 The ALICE experiment

3.1 The Large Hadron Collider

The Large Hadron Collider (LHC) is a particle collider located at the European Organization for Nuclear Research (CERN) and lies under the Franco-Swiss border, at a depth of 175 meters as seen in figure 3.1. It is a 27 kilometers in circumference tunnel, where two counter-rotating beams collide in four different points corresponding to four main experiments: CMS (Compact Muon Solenoid), ATLAS (A Toroidal LHC ApparatuS), LHCb (Large Hadron Collider beauty) and ALICE (A Large Ion Collider Experiment). The LHC started to function for the first time on 2009 with a 0.9 TeV center-of-mass energy, and progressivly reached 8 TeV in 2012 during the run I. In run II (which started on april 2015) it will reach a 13 TeV center-of-mass energy.

The LHC uses state-of-the-art technologies, including supraconductor magnets cooled down to 2 K by superfluid helium. These magnets deliver a powerful and almost constant 8 T magnetic induction to guide the beams inside the tubes, and radio-frequency systems to accelerate the particles. It uses previous CERN particle colliders (one of them being the SPS, Super Proton Synchrotron that started to acquire data in 1976, and which can be seen in figure 3.1) as the first steps in the injection process of the beams into the LHC tubes, accelerating them progressively.

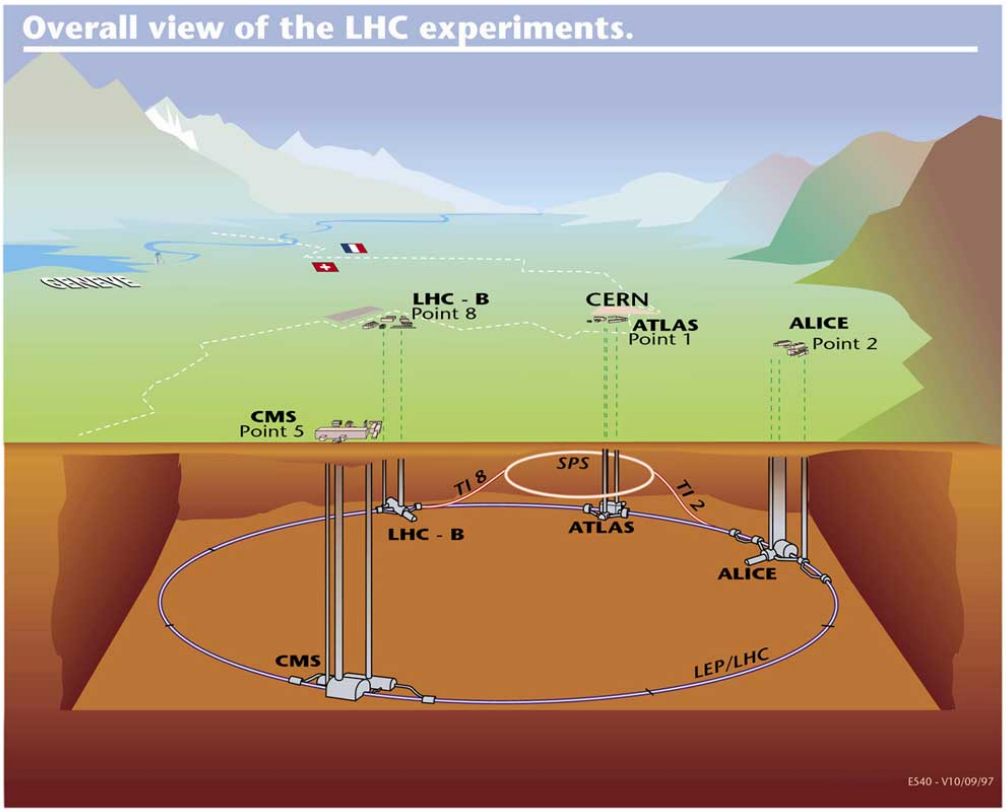

Figure 3.1: The Large Hadron Collider. Note that the Super Proton Synchrotron (SPS), another particle collider, is visible in this figure, as it is used to inject the beams into the LHC tubes. The four main LHC experiments are also shown (CMS, ATLAS, LHCb, and ALICE).

3.2 The ALICE experiment

The ALICE experiment has as a main objective the study of the QGP, recreated with heavy ion collisions. ALICE is divided in two parts: a central barrel and a muon spectrometer. The central barrel, is located at mid rapidity ($-0.9 < y < 0.9$) while the muon spect is located at forward rapidity ($-4 < y < -2.5$). The ALICE experiment, as it was during the LHC Run I, can be seen in figure 3.2.

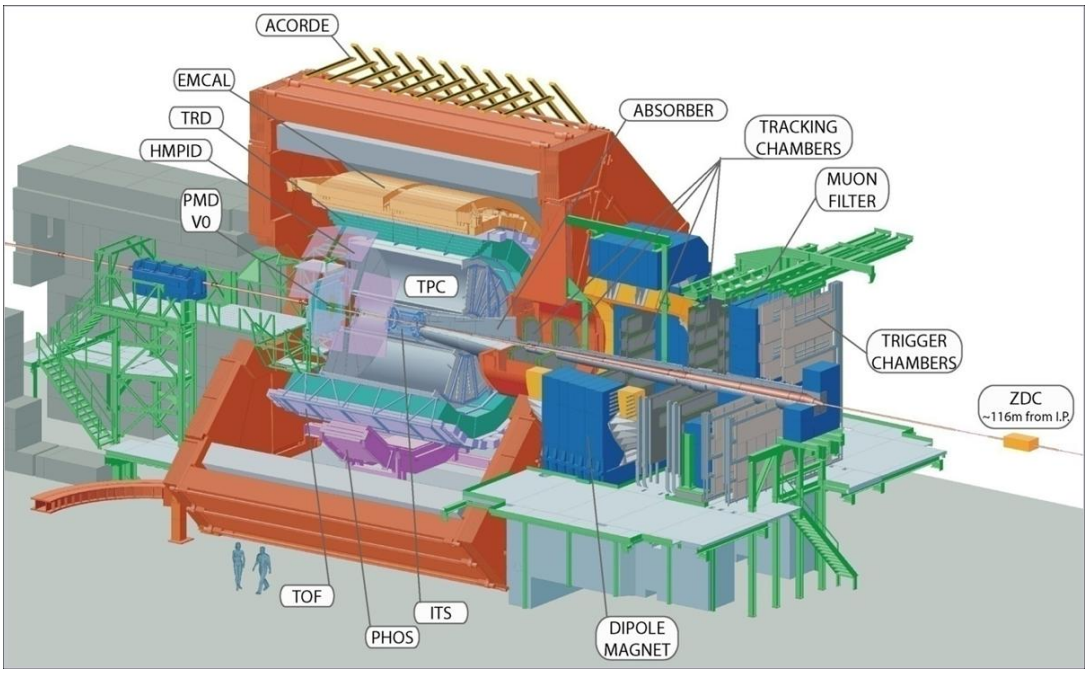

Figure 3.2: The ALICE experiment during the Run I. The central barrel is inside the solenoid L3 magnet in red. The muon spectrometer is on the right side.

The central barrel of the ALICE experiment features several detectors: the Inner Tracking System (ITS), a Time Projection Chamber (TPC), the Transition Radiation Detector (TRD), the Time-Of-Flight (TOF), the High Momentum Particle Identification Detector (HMPID), the PHOtom Spectrometer (PHOS) and the ElectroMagnetic Calorimeter (EMCal).

In this study, we'll only use one of these detectors: the ITS. All details about the other central barrel detectors are available in [6].

3.2.1 The upgrade of the ITS

The ITS is located around the primary vertex and, among other characteristics, it measures the interaction point with great precision.

In this study, we used the upgraded version of the ITS. It features an inner barrel with three layers of detectors, the innermost covers a pseudorapdity range of $-2.5 < \eta < 2.5$. These inner barrel detectors have pixel size values of $(20 - 30) \times (20 - 30)$ μm^2.

The outer barrel has four layers of detectors, the outermost covers a pseudorapdity range of $-1.3 < \eta < 1.3$, and all of them feature pixels size of $(20 - 50) \times (20 - 50)$ μm^2.

All these six layers are equipped with pixel chips sharing the same technology: the 0.18 μm Complementary Metal Oxide Semi-conductor (CMOS) technology.

Another main modification is the reduction of the beampipe diameter, that was originally 29 mm, and in this upgraded version the value is 19.2 mm, reducing the particle scattering inside it.

All details about this upgraded ITS are available in [7], including all the technical aspects.

3.2.2 The muon spectrometer

The muon spectrometer is desingned for several types of studies: low mass resonances (ω, ρ and Φ), quarkonia (J/ψ, ψ', Υ, Υ', Υ'') and W/Z bosons through their dimuon decay channel ($\mu^+\mu^-$); open heavy flavors through semi-muonic decay channel as it is the case in this study; but also through $e-\mu$ coincidences with the muon detected in the muon spectrometer and the electron in the central barrel. The figure 3.3 shows in detail all its components.

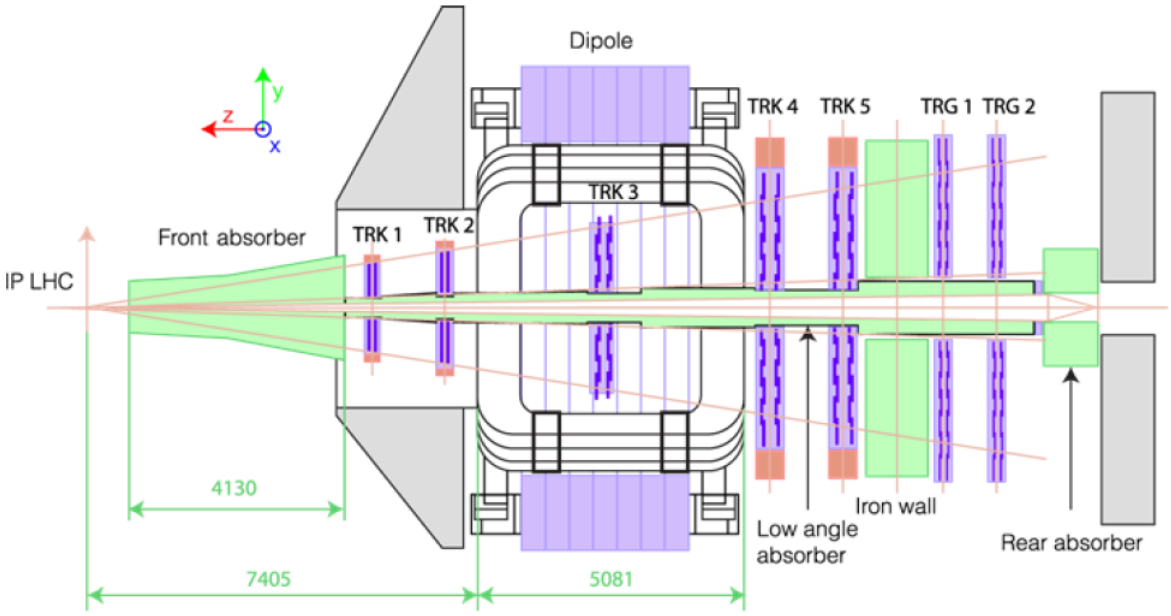

Figure 3.3: The muon spectrometer.

Absorbers

In central Pb-Pb collisions, there is a lot of background produced (hadrons and photons mainly). The absorbers protect the detectors from this.

The front absorber, situated at 90 cm of the nominal interaction point, is designed to absorb as soon as possible the many particles coming from the collision. Its presence also induces a lower limit on the muon impulsion of 4 GeV/c, the minimal value required to go through its total thickness.

The muon spectrometer also has others absorbers at various locations:

- The beam shield minimizes the background produced by the interactions with the beampipe.
- The iron wall, between the last tracking chamber and the first trigger chamber, stops hadrons that managed to punch through the front absorbers. As it is after the tracking chambers, it has no effect on their measures.

- The rear absorber protects the trigger chambers from backrgound produced by the accelerator (beam-gas interactions).

Tracking system

The five tracking stations, between the front absorber and the iron wall, detect particles and reconstruct their trajectories. Their surfaces increase along the z-axis in the direction of the trigger chambers, from 2.5 to 20 m^2. The total covered area is approximately 100 m^2. They use Multi-Wire Proportional Chambers (MWPC) with segmented cathodes called Cathode Pad Chambers (CPC). They all are filled with a mixture of two gas: 80 % Ar and 20 % CO_2.

The third tracking station (the middle one) is within a dipole magnet used to measure the muon's impulsion as they interact with the magnetic field produced by it. Depending on their impulsion and electrical charge, their trajectories are bent with a curvature radius (R) that follows:

$$R = p/|qB|$$

where B is the magnetic field of the dipole. Since the particles' trajectories are bent depending on their electrical charges, we can disitnguish muons (with a -1 e electrical charge) and anti-muons (that have an opposite charge). It is important in any physical study to have this information since, for example, the quarkonia decay into opposite signs muons. It is also important in our study, because we'll use this distinction later as a track selection.

Tigger system

Behind the iron wall, there are two trigger chambers made of Resistive Plate Chambers (RPC). They are used to select tracks based on their p_T. The background muons, coming mainly from kaons and pions, have low p_T values, and thus the associated background can be lowered. The trigger chambers can also select events that have muons of the same or opposite charges.

3.3 The Muon Forward Tracker (MFT)

3.3.1 The MFT working principle

As it is the case for many LHC experiments, it is planned to upgrade the detectors over the years. The Muon Forward Tracker (MFT) is one of the ALICE upgrades scheduled to be added during the second long shutdown, and it will become fully operational in run III.

The MFT is a set of five trackers that will be located before the front absorber of the muon spectrometer, between 50 and 76 cm from the interaction point, and thus much closer to the primary vertex than the already existing muon spectrometer trackers. The planes have outer radius ranging from 11 to 15.5 cm and all covering a pseudorapidity range of $-3.6 < \eta < -2.5$. Figure 3.4 shows the future muon spectrometer configuration (with the MFT) and also a closer and more detailed MFT figure.

Since the particle must pass through the $\sim$ 4.13 meters long front absrober, it degrades the information on their kinematics. Since the MFT is located before this absorber, the kinematics that are measured are much less degraded. Another limitation is that the distinction of beauty and charm hadrons is not possible with the current muon spectrometer setup, because of the front absorber presence and the great distance between the interaction point and the first of the five muon spectrometer's tracker. So the extrapolated tracks have uncertainties in the primary vertex area that are too large, preventing us from distinguishing beauty and charm. These are exaclty the limitations that the MFT will address.

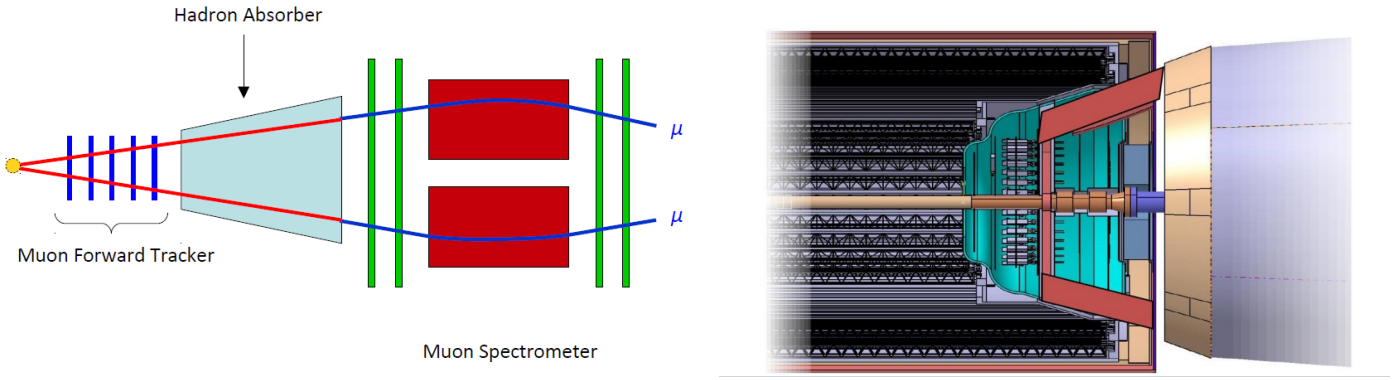

Figure 3.4: On the left, the muon spectrometer as it will be with the addition of the Muon Forward Tracker (MFT). On the right a closer look at the MFT in the middle. On the right in light blue is the front ansorber, on the left the future ITS detectors.

The MFT shares the same pixel technology than the future ITS upgraded detectors: CMOS Monolithic Active Pixels sensors with pixel pitch of 25 x 25 μm^2 and 50 μm thick, and they will be featured on all five tracking disks. That will allow a great precision tracking, as the MFT will be located in a region with high particle density, the resolution required in order to be able to distinguish these tracks is high. These pixels are integrated on a half-disk support by using a flexible printed circuit to form ladders. The ladders are then fixed onto a support and perpendicular to the half cone structure inner border. Figure 3.5 contains the detailed ladder and half disks. These five half disks are integrated into a half-cone made of carbon fiber, and are hermetically closed by kapton films around the structure, and a carbon fibre cover around the beampipe support. The whole detector will be cooled down using water cooling that will maintain the temperature around 35 °C. Finally the two half cones will be positionned and fixed to the beampipe support cage, one above it and one under it. Figure 3.5 shows a half cone, with the five half disks inside it.

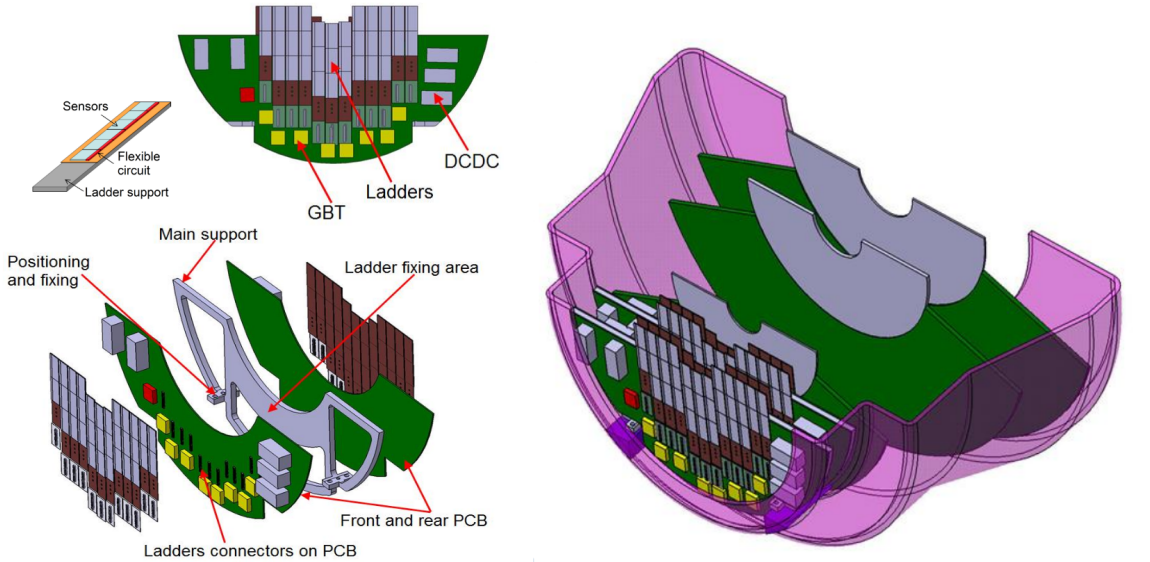

Figure 3.5: On the left, a half disk of the MFT. The pixels are put on ladders that are integrated on the half diks. On the right a MFT half cone, that will contain five half disks. One half cone will be put above the LHC beampipe and another one will be put under it.

The MFT will be part of the muon spectrometer, it will be used in a conjunction with the other pre-existent devices, including the five trackers located after the front absorber and the trigger chambers. The muon spectrometer will detect and reconstruct the trajectories of the particles that remain after the front absorber, and the two trigger chambers at the end will further reduce the background. With all these informations (MFT + muon spectrometer) we can select the MFT tracks that match the reconstructed tracks in the muon spectrometer (tracking tracks that match the trigger tracks). This way we are able to extrapolate the muon tracks to the primary vertex. The high precision muon tracks extrapolation is the key for this study: measuring their offsets with sufficient precision in order to be able to distinguish charm and beauty open heavy flavors. The offset is the distance, in the transverse plane of the collision, between the extrapolated muon track coordinates and the interaction point (primary vertex):

$$\text{Offset} = \sqrt{(x_{primary\ vertex} - x_{extrapolated\ muon\ track})^2 + (y_{primary\ vertex} - y_{extrapolated\ muon\ track})^2}$$

Due to their different mean lifetimes ($c\tau_D \approx 150$ μm and $c\tau_B \approx 500$ μm), the offset distributions of the muons coming from their decay can be used to distinguish them, as they'll be singificantly different in the two cases. The offset resolution depends on the p_T of the particle (~ 100 μm for $p_T = 0.5$ GeV/c and ~ 30 μm for $p_T = 5$ GeV/c)[8].

3.3.2 New measurements

By being closer to the primary vertex and used in conjunction with the rest of the muon spectrometer, the MFT will allow us to obtain much more precise muon track reconstructions, and thus muon tracks extrapolations. Table 3.1[9] lists a few observables and the impact of the MFT to their measures in the future, with the assumption of a 10 nb^{-1} integrated luminosity and for central Pb-Pb collisions. In the list, there are the expected performances for single muon open heavy flavor, but open heavy flavors can also be accessed via dimuons, and this is the subject of this masters report. The expected performance of the MFT for the single muon measurements has been recently updated[8]. The new open charm in single muon uncertainty at $p_T = 1$ GeV/c is $\sim$ 11 %. The p_T^{min} value for open beauty in single muon is now 3 GeV/c, with a total uncertainty of $\sim$ 8 %. Nevertheless, the table still illustrates the futur progresses thanks to the MFT for various measurements.

Observable	MUON only		MUON + MFT	
	p_T^{min} (Gev/c)	Uncertainty	p_T^{min} (Gev/c)	Uncertainty
Inclusive J/ψ R_{AA}	0	5% at 1 GeV/c	0	5% at 1 GeV/c
ψ' R_{AA}	0	30% at 1 GeV/c	0	10% at 1 GeV/c
Prompt J/ψ R_{AA}	–	not accessible	0	10% at 1 GeV/c
J/ψ from b-hadrons	–	not accessible	0	10% at 1 GeV/c
Open charm in single muon	–	–	1	7% at 1 GeV/c
Open beauty in single muon	–	–	2	10% at 2 GeV/c
Open Heavy Flavor in single muon (no charm/beauty separation)	4	30% at 4 GeV/c	–	–
Low mass spectral functions and QGP radiation	–	not accessible	1-2	20% at 1 GeV/c

Table 3.1: Comparison of physics reach for the two scenarios without (MUON only) and with the MFT (MUON + MFT), with an assumed integrated luminosity of 10 nb^{-1}, in central Pb-Pb collisions. The p_T^{min} column gives the minimum p_T value at which the measure is accessible. All uncertainties combine statistical and systematic uncertainties.

4 Dimuons from open heavy flavors with the MFT

The goal is to quantify the future MFT performances for the open heavy flavors measurements in the run III. The procedure is to start from a Monte-Carlo simulation of 1.4×10^6 0-10% central Pb-Pb collisions in the ALICE experiment with the expected conditions of run III: a center-of-mass energy of $\sqrt{s_{NN}} = 5.5$ TeV and equipped with the upgraded ITS and the MFT. From this simulation we extract the offset and weighted offset distributions in order to disentangle the muon sources in different invariant mass regions and dimuon p_T ($p_T^{\mu\mu}$) ranges. We evaluate the systematic uncertainties coming from the detector and the Monte-Carlo effects.

4.1 Definitions

4.1.1 Offset and weighted offset

In addition to the offset, the weighted offset is another very useful observable. It is defined as the offset weighted by the uncertainty on the track extrapolation.

Now that the single muon offset and weighted offset are defined, we need to define the dimuon offset and weighted offset. The dimuon offset is given by the quadratic sum of the single muons' offsets:

$$\text{Dimuon offset} = \sqrt{(\text{Offset } \mu_1)^2 + (\text{Offset } \mu_2)^2}$$

The dimuon weighted offset is defined in a similar way to the dimuon offset.

4.1.2 Signal, background, invariant mass regions and dimuon p_T ranges

The central Pb-Pb collisions was simulated using HIJING. However, producing an enough amount of heavy quarks would require to generate an incredible amount of events. To solve this problem heavy quarks are produced, via AliGenCorrHF, on top of the HIJING simulation. This implies the necessity to define the particles that will be used as signal and those that will be used as background.

Signal and background

For this study, we'll only use the semi-muonic decay channels: open heavy flavors that decay into $\mu^{\pm}$ + X, with X any other kind of particle. In addition to that, and only for the open beauty, we'll also include muons coming from chain decay. The signal can be:

- "direct b": pairs of muons that both directly come from the decay of beauty hadrons;
- "direct d": pairs of muons that both directly come from the decay of charm hadrons;
- "chain b": pairs of muons that both come from the chain decay of beauty hadrons, or pairs of muons in which one comes from a chain decay of a beauty hadron and the other directly from the decay of a beauty hadron;

In the three cases, the particles should be generated by AliGenCorrHF.

We have three background sources:

- "chain d": pairs of muons that both come from the chain decay of charm hadrons, or pairs of muons in which one comes from a chain decay of a charm hadron and the other directly from the decay of a charm hadron;
- "resonances": pairs of muons that both directly come from the decay of a resonance;
- "background": any combination of muons that are not "direct b", "direct d", "chain b", "chain d" nor "resonances" (for example the combination of a muon coming from "direct b" and "resonances");

In the three cases, the particles should be generated by HIJING.

Mass regions

We'll divide our study in two invariant mass regions:

- A low mass region: $1.2 < M_{\mu\mu} < 2.8$ GeV/c^2;
- A high mass region: $4 < M_{\mu\mu} < 9$ GeV/c^2;

This way, we avoid the low mass resonances (ω. ρ, and Φ) in $M_{\mu\mu} < 1.2$ GeV/c^2, the J/ψ and ψ' resonances between 2.8 and 4 GeV/c^2, and the Υ family above 9 GeV/c^2[2].

$p_T^{\mu\mu}$ ranges

This study has been divided into several $p_T^{\mu\mu}$ ranges for the low mass region, which are:

- $p_T^{\mu\mu} = 0 - 1$ GeV/c;
- $p_T^{\mu\mu} = 1 - 2$ GeV/c;
- $p_T^{\mu\mu} = 2 - 3$ GeV/c;
- $p_T^{\mu\mu} = 3 - 5$ GeV/c;

In the high mass region, due to the lack of statistic, there will only be one dimuon p_T range: $p_T^{\mu\mu} = 0 - 5$ GeV/c.

4.2 Selection criteria

In the simulation, the background represents the majority of the reconstructed muons/dimuons: it is more than 98% of the total statistic. In order to reduce this proportion, we'll perform several cuts, at the single muon and dimuon levels.

4.2.1 Single muon and dimuon cuts

There are four single muon cuts:

- Pseudorapidity cut: $-3.6 < \eta < -2.5$;
- Matching between the MFT and the muon spectrometer tracks with the trigger tracks;
- The χ^2 divided by the Number of Degrees Of Freedom ($NDOF$) obtained for the track reconstruction must be smaller than 3: $\chi^2/NDOF < 3$;
- All single muon p_T must be larger than 0.5 GeV/c: $p_T^{\mu} > 0.5$ GeV/c;

The plot on the left in figure 4.1 shows the $p_T^{\mu\mu}$ distributions without any cut, the plot on the right shows the $p_T^{\mu\mu}$ distributions with all the single muon cuts enabled.

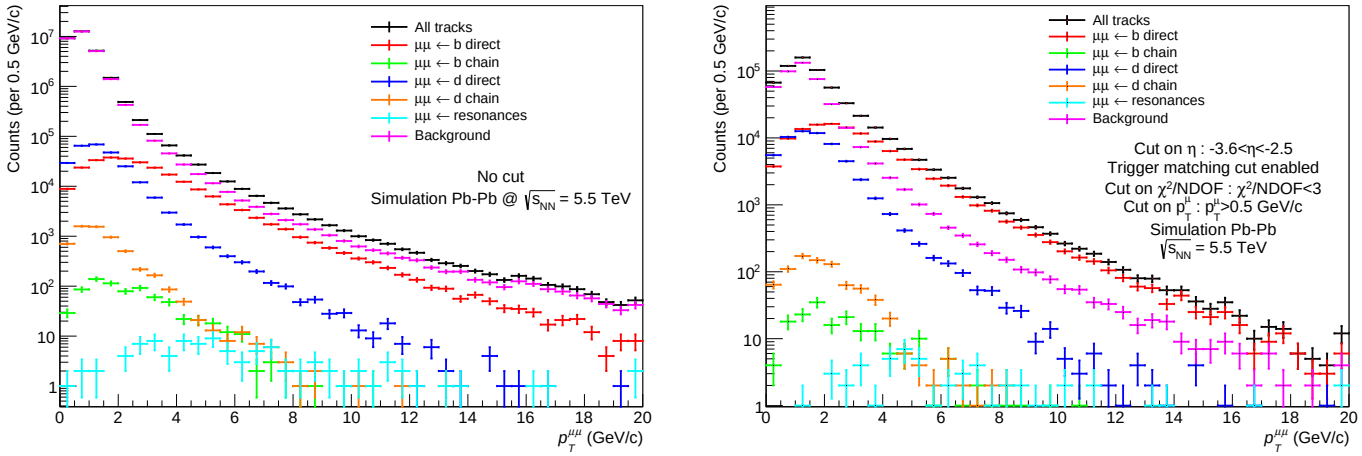

Figure 4.1: $p_T^{\mu\mu}$ distributions for each source wihtout any cut (*left*), the background is dominating. $p_T^{\mu\mu}$ distributions for each source after applying all the single muon cuts (*right*), the background has been reduced. Note that all of these $p_T^{\mu\mu}$ distributions are not scaled to an integrated luminosity of 10 nb^{-1}.

At the dimuon level, we'll only select pairs of muons that have opposite electrical charges ($\mu^+\mu^-$). Thanks to this cut, we reduce the background even further: only 49.75% of the background tracks that remained after the four single muon cuts are still present after this dimuon cut.

4.2.2 Impact of the cuts

Table 4.1 shows the evolution of the proportion for each source after the single muon and dimuon cuts. The background has been considerably reduced from $\sim$ 98% to $\sim$ 60%, and the signals in the other hand have risen in proportions, especially the "direct b" and "direct d" that increased from less than 1% each one to $\sim$ 25% for the first and $\sim$ 15% for the second.

Source	Proportion of the total statistic (%) after the succesive cuts				
	No cut	η and matching	η, matching and χ^2	η, matching, χ^2 and p_T^μ	η, matching, χ^2, p_T^μ and opposite sign muons
Direct b	0.8760	8.5961	12.1007	19.4726	25.5458
Direct d	0.8989	4.7974	6.6812	9.6144	15.1424
Chain b	0.0026	0.0151	0.0204	0.0294	0.0218
Chain d	0.0199	0.0745	0.1036	0.1357	0.1226
Resonances	0.0003	0.0039	0.0055	0.0090	0.0151
Background	98.2041	86.5302	81.0915	70.7427	59.1523

Table 4.1: Table of the proportions for each source after the single muon and dimuon cuts: "η" refers to the pseudorapidity cut (-3.6 < η < -2.5), "matching" is the matching between the MFT and muon spectrometer tracks with the trigger tracks, "χ^2" is the cut on $\chi^2/NDOF$ ($\chi^2/NDOF < 3$), "p_T^μ" is the cut on the single muon p_T ($p_T^\mu > 0.5$ GeV/c), and "opposite charge muons" is the dimuon cut: we only select pair of muons with opposite electric charges ($\mu^+\mu^-$).

4.3 Reference charm, beauty and background templates

For the sake of simplicity we will regroup the six sources defined earlier into three categories:

- "beauty" is the sum of "direct b" and "chain b";
- "charm" is the new name of "direct d";
- "background" is the sum of "chain d", "resonances" and the previously defined "background";

Reference templates

We need to build the beauty, charm and background "reference" dimuon offset and weighted offset templates from the Monte-Carlo simulation. This process takes several steps, which are the same for all three sources:

- Parametrization of the offset distribution;
- Smooth the resulting histogram from the parametrization function;
- Normalization of the "smoothed" histogram to one;
- Scaling the "smoothed" histogram to the expected statistic assuming a 10 nb^{-1} integrated luminosity;
- Adding the three "smoothed" histograms into a fourth one called "total" reference template;

We'll perform all of these steps for the two cases: offset and weighted offset distributions, and for all $p_T^{\mu\mu}$ ranges in both mass regions.

Parametrization

The first step is the parametrization of the dimuon offset and weighted offset distrbutions. For this we'll use a Variable Width Gaussian as a parametrization function, where the width is a ploynomial function of the offset or weighted offset. The fitting criteria are:

- We require a "CONVERGED" status;
- The $\chi^2/NDOF$ value must be lower than 2: $\chi^2/NDOF < 2$;
- The "ERROR MATRIX" value must be lower than 5%: ERROR MATRIX $< 5\%$;

Smoothing and scaling

Once we have the parametrization functions, we create a "smoothed" histogram from them, by dividing the offset interval into small bins and filling the histogram with the parametrization function value in the center of each bin. In this way, any residual fluctuation coming from the limited Monte-Carlo sample can be removed. This "smoothed" histogram is then normalized to one.

After this we scale the histogram to the expected statistics for an integrated luminosity of 10 nb^{-1}. The values corresponding to 10 nb^{-1} are in the table 4.2[9]. The reason for this is that the expected number of 0-10% Pb-Pb collisions for the run III of ALICE is 7.7×10^9[9]. However, the present analysis was performed using only 1.4×10^6 0-10% central Pb-Pb collisions, which makes the scaling necessary.

Figure 4.2 shows all the reference offset templates in the low mass region for all four $p_T^{\mu\mu}$ ranges.

Figure 4.3 shows all the reference weighted offset templates for the low mass region for all four $p_T^{\mu\mu}$ ranges.

Figure 4.4 shows the reference offset and weighted offset templates for the high mass region.

Low mass region				High mass region			
$p_T^{\mu\mu}$ (GeV/c)	statistic ($\times 10^3$)			$p_T^{\mu\mu}$ (GeV/c)	statistic ($\times 10^3$)		
	beauty	charm	background		beauty	charm	background
0-1	36	1 400	15 800	0-5	606	652	5 442
1-2	76	1 940	24 800				
2-3	124	1 300	19 600				
3-5	192	593	9 470				

Table 4.2: Expected statistics for the three sources, assuming an integrated luminosity of 10 nb^{-1}, for all $p_T^{\mu\mu}$ ranges and both mass regions[9].

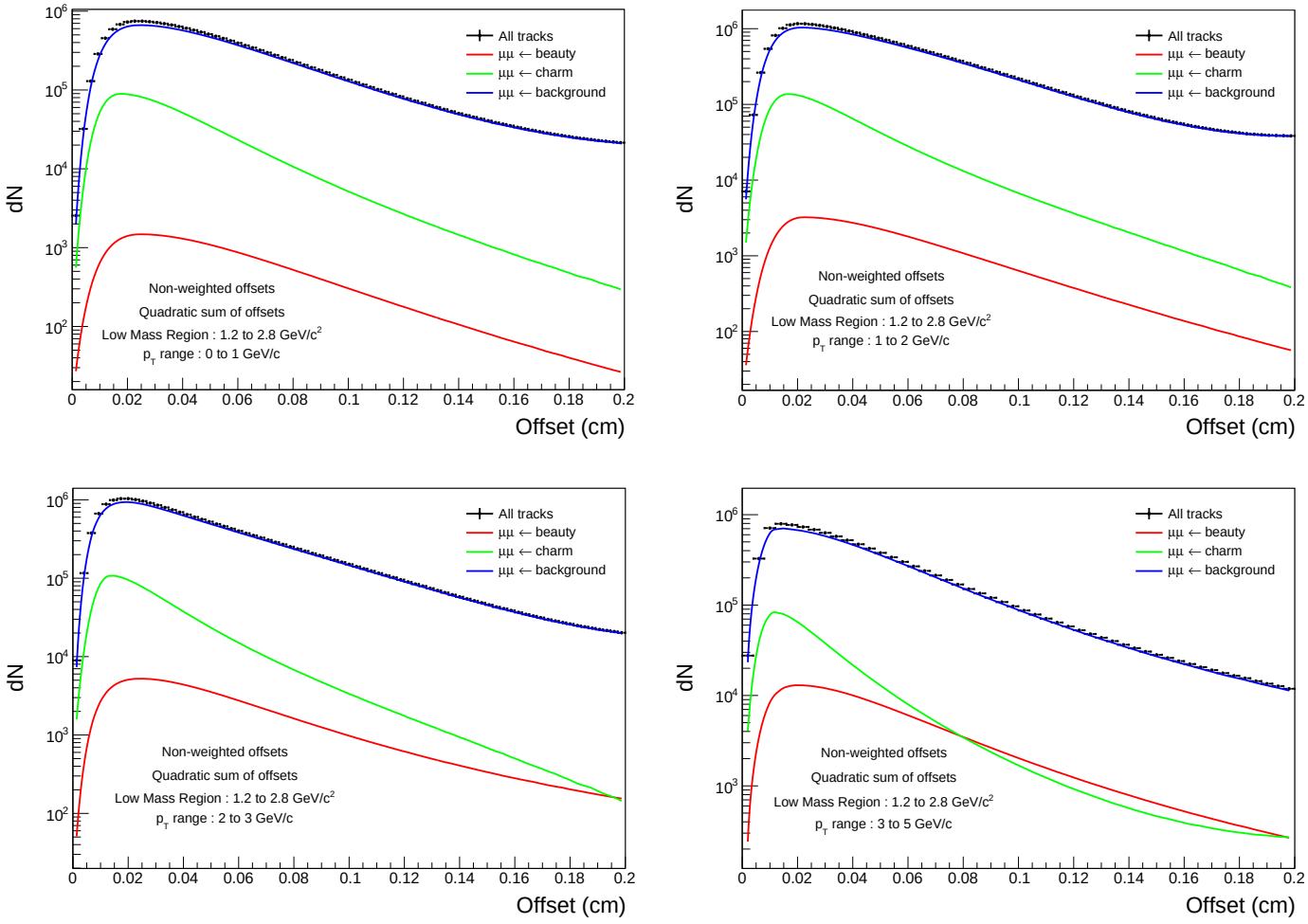

Figure 4.2: Reference offset templates in the low mass region for each source. The $p_T^{\mu\mu}$ ranges are: 0 to 1 GeV/c (*top left*), 1 to 2 GeV/c (*top right*), 2 to 3 GeV/c (*bottom left*) and 3 to 5 GeV/c (*bottom right*). Note that all of these offset distributions are scaled to an integrated luminosity of 10 nb^{-1}.

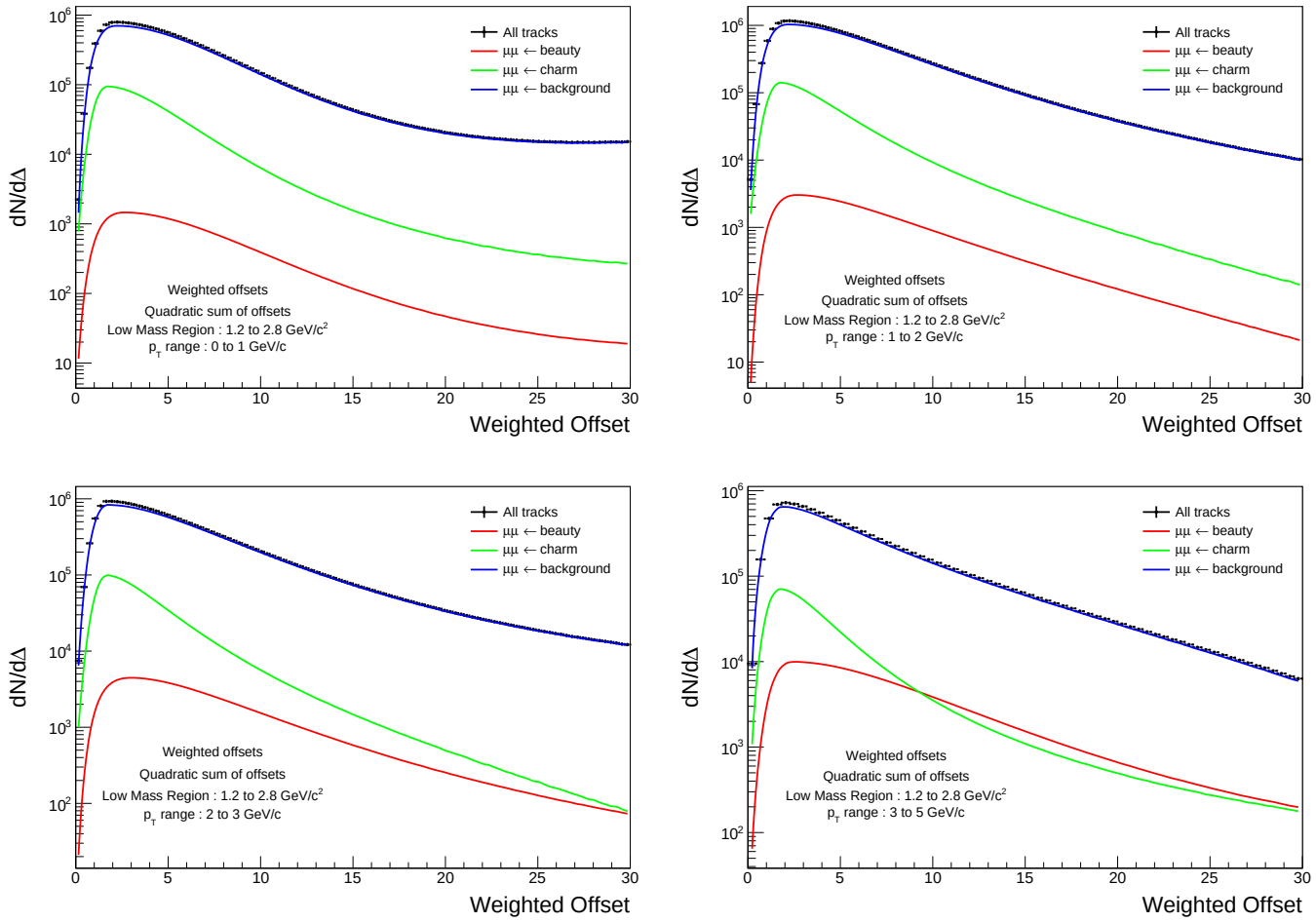

Figure 4.3: Reference weighted offset templates for the low mass region for the $p_T^{\mu\mu}$ ranges: 0 to 1 GeV/c (*top left*), 1 to 2 GeV/c (*top right*), 2 to 3 GeV/c (*bottom left*) and 3 to 5 GeV/c (*bottom right*). Note that all of these weighted offset distributions are scaled to an integrated luminosity of 10 nb^{-1}.

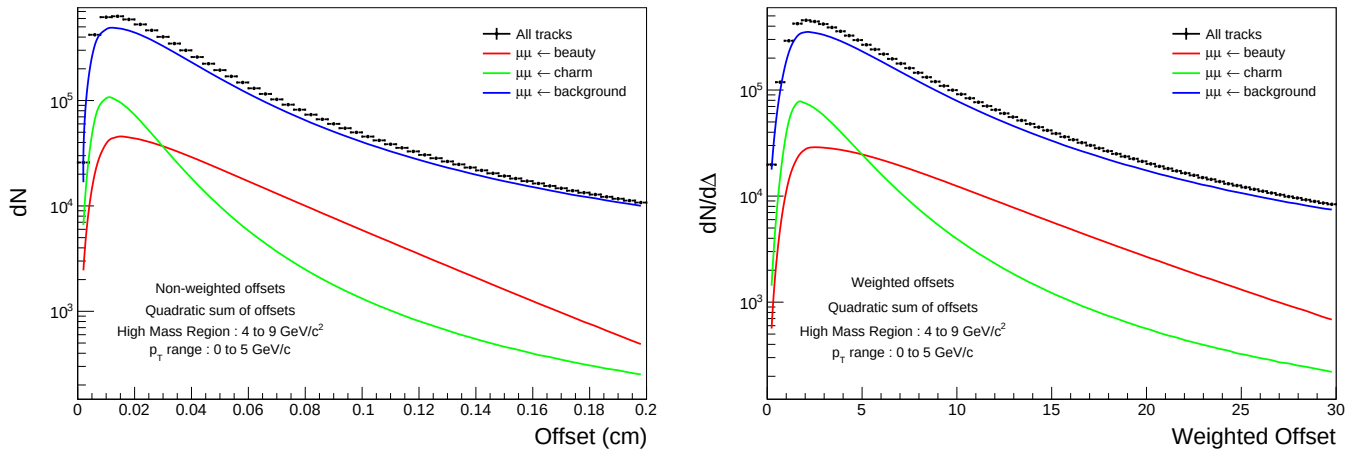

Figure 4.4: Refrence offset (*left*) and weighted offset (*right*) templates for the high mass region for the $p_T^{\mu\mu}$ range 0 to 5 GeV/c. Note that all of these offset and weighted offset distributions are scaled to an integrated luminosity of 10 nb^{-1}.

Invariant mass analysis

In addition to the offset, there exists another observable that can be used to distinguish open beauty and open charm: the invariant mass distributions. We performed the same analysis as described above for the offset and weighted offset but for the invariant mass distributions, in both mass regions. The steps are the same: we apply the same single muon and dimuon cuts, parametrization, smoothing and scaling to the expected statistic with a 10 nb^{-1} integrated luminosity. The smoothed invariant mass templates for both mass regions are shown in figure 4.5.

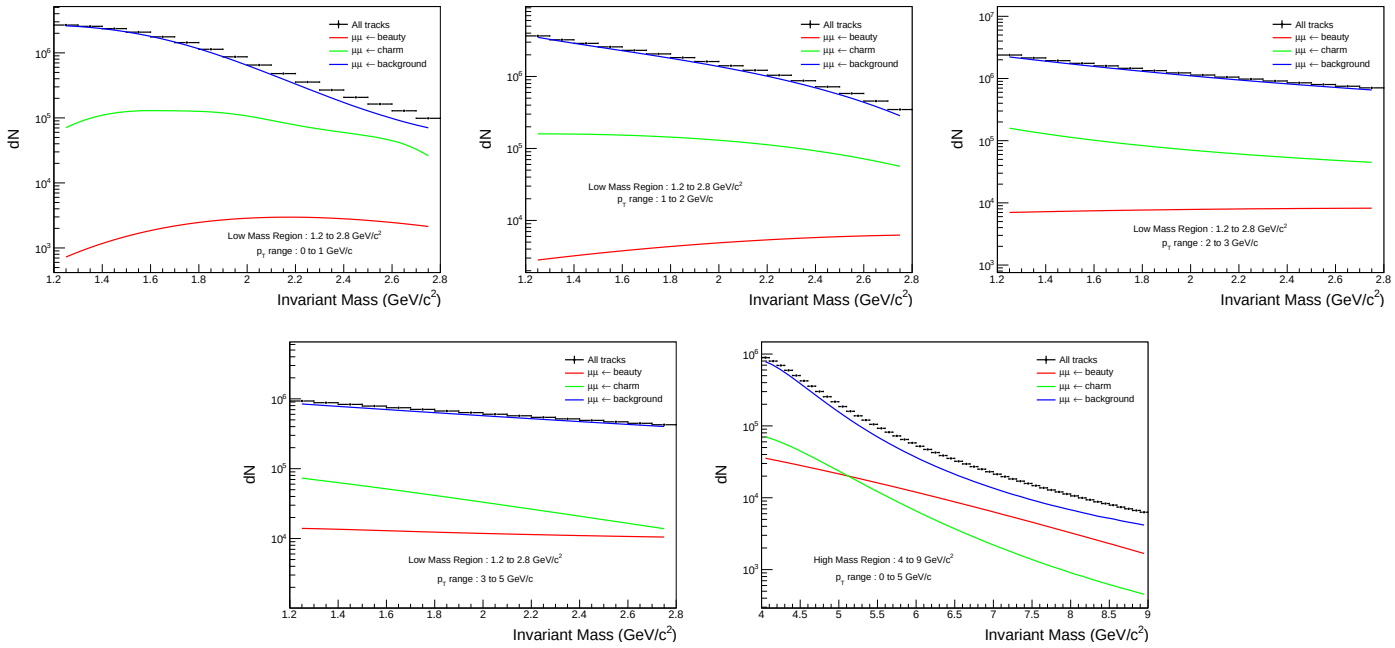

Figure 4.5: Reference invariant mass templates in both mass regions for each source. The three top plots and the bottom left plot are for the low mass region, in the $p_T^{\mu\mu}$ ranges: 0 to 1 (*top left*), 1 to 2 (*top middle*), 2 to 3 (*top right*) and 3 to 5 GeV/c (*bottom left*). On the bottom right are the distributions for the high mass region, in the $p_T^{\mu\mu}$ range 0 to 5 GeV/c. Note that all of these invariant mass distributions are scaled to an integrated luminosity of 10 nb^{-1}.

4.4 Uncertainties estimation

In order to determine which observable (offset or weighted offset) is the best suited to distinguish open beauty and open charm, we need to evaluate the uncertainties for each one. This way, we'll chose the observable that gives the smallest uncertainties, and so, will be the most accurate for the open beauty/charm distinction. The total uncertainties in each case are the quadratic sums of the statistical errors and all the systematic uncertainties.

4.4.1 Systematic uncertainties

We have three sources of systematic uncertainties:

- A misalignement between the ITS and the MFT;
- The limited MFT pointing accuracy;
- Different Monte-Carlo inputs;

For each of them we'll re-compute all the single muon offsets and weighted offsets but with a different configuration that depends on the source of the systematic uncertainty. From there we re-compute a set of distorted dimuon offsets and weighted offsets, and then we divide them by the reference ones (Distorted/Reference). Then we parametrize this ratio using polynomial functions, and we use these functions to deform the reference templates. Some of the systematic uncertainties described in the following have ratios in $p_T^{\mu\mu}$ ranges that cover more than one of the $p_T^{\mu\mu}$ bin from section 4.1.2, in these cases, the same parametrization function is used across all the reference $p_T^{\mu\mu}$ bins that are covered. For example if the ratio is performed for $p_T^{\mu\mu}$ = 2-5 GeV/c, then the parametrization function obtained will be multiplied by both "reference" templates for $p_T^{\mu\mu}$ = 2-3 GeV/c and $p_T^{\mu\mu}$ = 3-5 GeV/c ranges.

In the high mass region, for the ITS-MFT misalignement and MFT pointing accuracy systematic uncertainties, and due to the lack of statistic, we performed the ratios for the sum of the charm and the background. However, this is the case only for the ratios: we applied the same fit function to distort separately the charm and background "reference" templates.

ITS-MFT misalignment

We chose a realistic 10 μm misalignment between the MFT and the ITS. The primary vertex coordinates are shifted by 10 μm in both x and y directions, and in two cases, either + or - 10 μm:

$$\text{First case: } \begin{cases} \mathrm{x}_{vertex} \rightarrow x_{vertex} + 10\ \mu\mathrm{m} \\ \mathrm{y}_{vertex} \rightarrow y_{vertex} + 10\ \mu\mathrm{m} \end{cases} \qquad \text{Second case: } \begin{cases} \mathrm{x}_{vertex} \rightarrow x_{vertex} - 10\ \mu\mathrm{m} \\ \mathrm{y}_{vertex} \rightarrow y_{vertex} - 10\ \mu\mathrm{m} \end{cases}$$

We performed this analysis in a 0 to 5 GeV/c $p_T^{\mu\mu}$ range, in both mass regions and for both offset and weighted offset distributions, as the misalignment does not depend on the p_T of the tracks. A few parametrizations of the ratios Distorted/Reference are shown in figure 4.6.

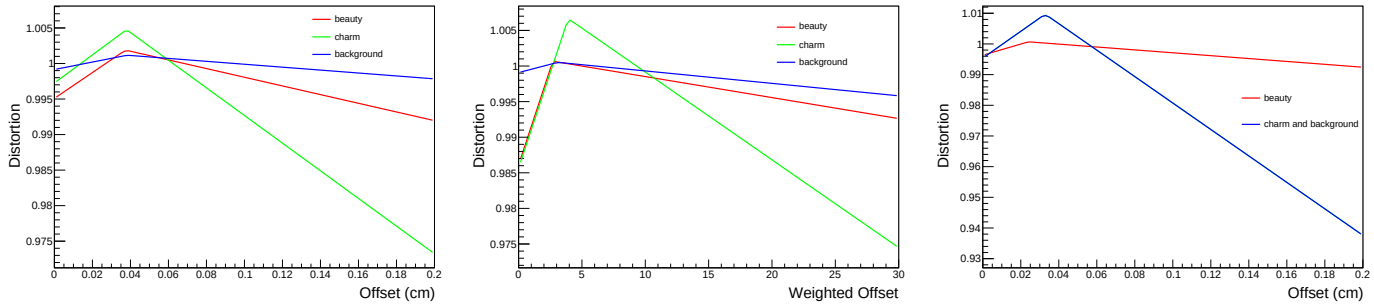

Figure 4.6: Examples of the parametrizations Distorted/Reference for the ITS-MFT misalignment systematic uncertainty for the three sources, in the $p_T^{\mu\mu}$ range 0 to 5 GeV/c and for a + 10 μm misalignment. The left and middle plots are for the low mass region: for the offset (*left*) and the weighted offset (*middle*). The plot on the right is for the offset in the high mass region. In the high mass region the parametrization, in order to constraint the fit, corresponds to the sum of charm and background contributions.

MFT pointing accuracy

The MFT will have a limited pointing accuracy that will depend on the single muons' p_T. The figure 4.7 shows the future MFT pointing accuracy resolution, in both x and y directions, as a function of the p_T^{μ}. To reproduce this effect, we smeared the single muons' coordinates x and y in the transverse plane using a Gaussian function with a p_T^{μ} dependent width that reflects the MFT pointing accuracy. We take as

a width one third of the MFT pointing accuracy in each p_T^μ range, in order to cover the MFT pointing accuracy within three sigmas, which represents more than 99.7% of the cases. These widths are listed in the table 4.3.

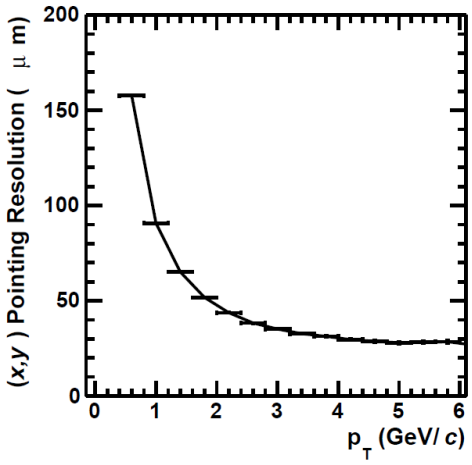

Figure 4.7: The MFT pointing accuracy as a function of the single muon p_T (p_T^μ), in both x and y directions[8].

p_T^μ (GeV/c)	σ (μm)
0.5 to 1	40
1 to 1.5	30
1.5 to 3	20
> 3	10

Table 4.3: Gaussian widths for the muon track smearing chosen in each single muon p_T range.

In the low mass region, we performed the ratios for several $p_T^{\mu\mu}$ ranges, but we need enough statistic in order to constraint the parametrizations to the ratios Distorted/Reference, so we have chosen these $p_T^{\mu\mu}$ ranges:

- beauty: 0-3 and 3-5 GeV/c;
- charm and background: 0-1, 1-2 and 2-5 GeV/c;

In the high mass region, the only $p_T^{\mu\mu}$ range is: 0 to 5 GeV/c. A few parametrizations of the ratios Distorted/Reference are shown in figure 4.8.

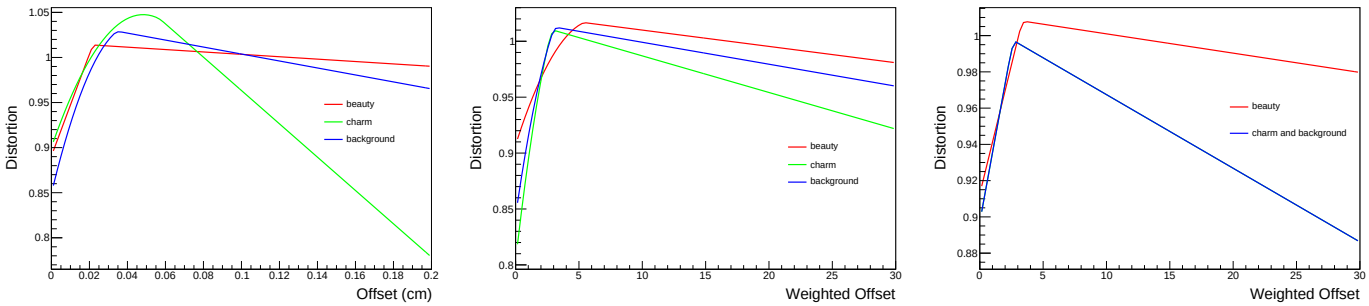

Figure 4.8: Examples of the parametrizations Distorted/Reference for the MFT pointing accuracy systematic uncertainty for the three sources. The left and middle plots are for the low mass region in the $p_T^{\mu\mu}$ range 3 to 5 GeV/c: for the offset (*left*) and the weighted offset (*middle*). The plot on the right is for the weighted offset in the high mass region and in the $p_T^{\mu\mu}$ range 0 to 5 GeV/c. In the high mass region, charm and background are added in order to obtain a unique parametrization.

Monte-Carlo inputs

We used as Monte-Carlo generators AliGenCorrHF and HIJING, but there exist other event generators for the same processes. In order to quantify the systematic uncertainties coming from these different

Monte-Carlo inputs, we will weight, at the single muon level, the charm and beauty offset and weighted offset distributions as:

$$\text{Weight} = (\text{FONLL/AliGenCorrHF}) \times R_{AA}(\text{alternative model})$$

where FONLL means "Fixed Order Next to Leading Log" and is a pQCD model for heavy quark production, AliGenCorrHF is the generator we use for the open heavy flavors and the R_{AA}(alternative model) is the nuclear modification factor of an alternative model for a given source (open beauty or open charm). The FONLL framework has proven to be successful to predict heavy quark production in proton-proton collisions[10]. The R_{AA} models take into account heavy ion collisions' nuclear effects (radiative and/or collisional energy loss). The R_{AA} plots for each alternative models are available in figures A.13, A.14, A.15 and A.16 in the appendix. The list of alternative models that we used for beauty and charm are:

- beauty: Uphoff, HeM, HTLTH155;
- charm: POWLANG, MCHQEPOS and MCHQEPOSRadLPM;

The "reference" histograms, only for the Monte-Carlo inputs systematic uncertainties and only for the beauty and the charm, are no longer the ones described in section 4.3, but the ones obtained by applying the weight with the following models:

- beauty: LatQCDTH155;
- charm: TAMU;

We chose those models because they have the best descriptions of the ALICE data. The LatQCDTH155 and TAMU offset and weighted offset distributions have been processed with the same approach as described earlier for the "reference" templates: parametrization, smoothing and scaling to 10 nb^{-1} in both mass regions and across all $p_T^{\mu\mu}$ ranges.

For the background, since it is composed of a lot of different kind of particles, there is no global model for it. We used as "reference" histograms for the background the distributions obtained without any distortion (section 4.3). To obtain the two "alternative models" for the background, we applied these weights at the single muon level:

- First weight: $0.5 + (1/10 \cdot p_T^{\mu})$;
- Second weight: $1.5 - (1/10 \cdot p_T^{\mu})$;

Finally, the weight at the dimuon level, for the three sources, is the multiplication of the two single muon weights that form the pair: (weight μ_1) $\cdot$ (weight μ_2).

Then we divide the offset and weighted offset distributions obtained with a different model by the "reference" distributions. We select in each case the alternative model that gives the largest deviation from unity and parametrize the corresponding ratio with polynomial functions. The models that gave the largest deviations are:

- For the beauty: Uphoff;
- For the charm: POWLANG, except for the offset in the $p_T^{\mu\mu}$ range 1-2 GeV/c and the weighted offset in $p_T^{\mu\mu}$ range 2-5 GeV/c in which it is for the two cases MCHQEPOSRadLPM;
- For the background: $0.5 + (1/10 \cdot p_T^{\mu})$;

The $p_T^{\mu\mu}$ range in which we perfomed the ratios are: in the low mass region we chose 0-3 anf 3-5 GeV/c

for the beauty and 0-1, 1-2 and 2-5 GeV/c for the charm and the background; in the high mass region it is 0 to 5 GeV/c in all cases.

Figure 4.9 shows a few parametrizations of the ratios Distorted/Reference.

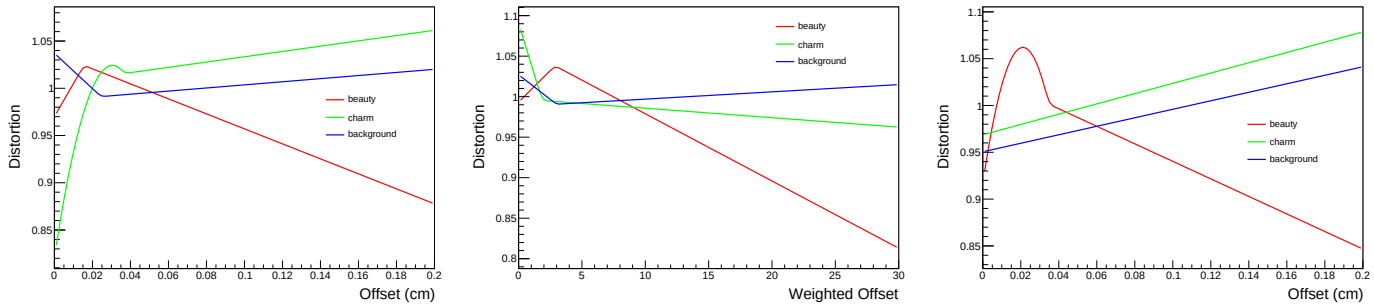

Figure 4.9: Examples of the parametrizations Distorted/Reference for the Monte-Carlo input systematic uncertainties for the three sources. The plots on the left and in the middle are for the low mass region, in the $p_T^{\mu\mu}$ range 3 to 5 GeV/c: for the offset (*left*) and the weighted offset (*middle*). The plot on the right is for the offset in the high mass region, in the $p_T^{\mu\mu}$ range 0 to 5 GeV/c.

Final step

We obtain the "distorted" templates, for each systematic uncertainty source, mass region and $p_T^{\mu\mu}$ range, by mutliplying the parametrized ratios Distorted/Reference by the "reference" templates.

These "distorted" templates are then used to fit the total reference (sum of charm, beauty and background) offset and weighted offset distributions in each $p_T^{\mu\mu}$ range. The fit function is the superposition of the three expected constributions:

$$F = C \cdot f_{charm} + B \cdot f_{beauty} + D \cdot f_{background} \tag{4.1}$$

where f_{charm}, f_{beauty} and $f_{background}$ are the "distorted" templates for charm, beauty and background respectively. In the same way, B, C and D are the free parameters corresponding to the normalization of the three components.

The systematic uncertainties are then obtained for the beauty and the charm as:

$$\text{Systematic uncertainty} = |1 - \frac{\text{(Integral of the distorted distribution)}}{\text{(Integral of the reference distribution)}}|$$

In the end the total systematic uncertainty is the quadratic sum of the three systematic uncertainties.

4.4.2 Statistical errors

In addition to the systematic uncertainties we also need to quantify the statistical errors. We'll use a similar approach as for the systematic uncertainties: we fit the total "reference" distribution using function 4.1 that is now the sum of the three "reference" components and not the "distorted" ones. We evaluate the statistical errors as:

$$\text{Statistical error} = \text{(Parameter error)/(Integral of the reference distribution)}$$

5 Results

We'll present and discuss the statistical errors, the systematic uncertainties and the total uncertainties, for each source, each $p_T^{\mu\mu}$ range and mass region.

5.1 Statistical errors and systematic uncertainties

Systematic uncertainties

All the systematic uncertainties, for the low mass region, are shown in table 5.1 (offset) and in table 5.2 (weighted offset). Table 5.3 contains all the systematic uncertainties for the high mass region.

$p_T^{\mu\mu}$ (GeV/c)	Systematic uncertainties for the offset in the low mass region							
	ITS-MFT misalignment				MFT pointing accuracy		Monte-Carlo inputs	
	beauty		charm		beauty	charm	beauty	charm
	+10μm	-10μm	+10μm	-10μm				
0-1	95.5%	–	0.5%	**8.4**%	–	65.9%	–	7.1%
1-2	–	–	0.6%	**8.6**%	–	51.4%	–	13.7%
2-3	–	–	3.4%	**5.6**%	–	67.0%	–	2.9%
3-5	30.5%	–	1.9%	**2.1**%	–	7.6%	–	2.5%

Table 5.1: Table of the systematic uncertainties in the low mass region for the offset. For each case, the largest ITS-MFT misalignment uncertainty is in bold. A hyphen indicates that uncertainty could not be quantified.

$p_T^{\mu\mu}$ (GeV/c)	Systematic uncertainties for the weighted offset in the low mass region							
	ITS-MFT misalignment				MFT pointing accuracy		Monte-Carlo inputs	
	beauty		charm		beauty	charm	beauty	charm
	+10μm	-10μm	+10μm	-10μm				
0-1	–	–	1.9%	**8.5**%	–	60.6%	–	11.0%
1-2	–	–	**3.2**%	3.0%	–	34.4%	–	0.6%
2-3	–	–	6.1%	**8.9**%	–	–	–	1.9%
3-5	34.6%	–	6.7%	**7.5**%	–	–	–	8.8%

Table 5.2: Table of the systematic uncertainties in the low mass region for the weighted offset. For each case, the largest ITS-MFT misalignment uncertainty is in bold. A hyphen indicates that uncertainty could not be quantified.

Observable	Systematic uncertainties in the high mass region ($p_T^{\mu\mu}$ range: 0-5 GeV/c)							
	ITS-MFT misalignment				MFT pointing accuracy		Monte-Carlo inputs	
	beauty		charm		beauty	charm	beauty	charm
	+10μm	-10μm	+10μm	-10μm				
Offset	**39.3**%	24.4%	**20.4**%	13.2%	–	45.7%	46.3%	27.7%
Weighted offset	**8.0**%	1.8%	**7.2**%	1.4%	3.6%	11.1%	22.6%	14.6%

Table 5.3: Table of the systematic uncertainties in the high mass region for the offset and weighted offset. For each case, the largest ITS-MFT misalignment uncertainty is in bold. A hyphen indicates that uncertainty could not be quantified.

Statistical errors and total systematic uncertainties

The statistical errors and the total systematic uncertainties for the low mass region are in table 5.4. The proper high mass region results are in table 5.5. For the ITS-MFT misalignment we have two cases: + 10 μm or - 10 μm. In order to be conservative, we'll pick, in each situation, the case that gives the largest systematic uncertainty.

Statistical errors and total systematic uncertainties in the low mass region								
$p_T^{\mu\mu}$ (GeV/c)	Offset				Weighted offset			
	Statistical errors		Total systematic uncertainties		Statistical errors		Total systematic uncertainties	
	beauty	charm	beauty	charm	beauty	charm	beauty	charm
0-1	–	0.7%	–	66.9%	–	1.0%	–	62.2%
1-2	81.8%	0.5%	–	53.9%	92.8%	0.9%	–	34.6%
2-3	55.7%	1.6%	–	67.3%	45.1%	1.8%	–	–
3-5	34.5%	2.8%	–	8.3%	23.6%	3.9%	–	–

Table 5.4: Table of the statistical errors and total systematic uncertainties in the low mass region for the offset and weighted offset. A hyphen indicates that uncertainty could not be quantified.

Statistical errors and total systematic uncertainties in the high mass region				
Observable	Statistical errors		Total systematic uncertainties	
	beauty	charm	beauty	charm
Offset	2.7%	1.1%	–	57.3%
Weighted offset	3.2%	1.7%	24.3%	19.8%

Table 5.5: Table of the statistical errors and total systematic uncertainties in the high mass region, in the $p_T^{\mu\mu}$ range 0-5 GeV/c and for the offset and weighted offset. A hyphen indicates that uncertainty could not be quantified.

Total uncertainties

The total uncertainties (quadratic sums of the statistical errors and total systematic uncertainties) for all cases are in table 5.6.

Total uncertainties in the low mass region					Total uncertainties in the high mass region				
$p_T^{\mu\mu}$ (GeV/c)	Offset		Weighted offset		$p_T^{\mu\mu}$ (GeV/c)	Offset		Weighted offset	
	beauty	charm	beauty	charm		beauty	charm	beauty	charm
0-1	–	67.0%	–	62.3%	0-5	–	57.4%	**24.6**%	**19.9**%
1-2	–	54.0%	–	34.7%					
2-3	–	67.4%	–	–					
3-5	–	**8.8**%	–	–					

Table 5.6: Table of the total uncertainties (statistical and systematic) in both mass regions and for the offset and weighted offset. A hyphen indicates that uncertainty could not be quantified.

5.2 Discussion

Low mass region

In the low mass region, in most cases the systematic uncertainties could not be determined or are very large, even for the ITS-MFT misalignment where the distortions are very small (as visible on the plots in figure 4.6), for both open beauty and open charm. In order to understand why, and given the fact that the background is dominating in every $p_T^{\mu\mu}$ range in the low mass region (as visible on the "reference" templates in figures 4.2 and 4.3 in section 4.3), we tried to evaluate its impact on the systematic uncertainties. We performed the same systematic uncertainties evaluation process described earlier for the ITS-MFT misalignment case, but this time we did not apply any distortion to the background. Table 5.7 shows the uncertainties obtained.

$p_T^{\mu\mu}$ (GeV/c)	ITS-MFT misalignment uncertainties wihtout background distortion							
	Offset				Weighted offset			
	beauty		charm		beauty		charm	
	+10μm	-10μm	+10μm	-10μm	+10μm	-10μm	+10μm	-10μm
0-1	2.6%	**48.3**%	0.4%	**0.6**%	**28.3**%	3.7%	0.4%	**0.6**%
1-2	58.0%	–	0.3%	**0.5**%	–	–	0.6%	**0.7**%
2-3	32.5%	**79.0**%	0.9%	**1.3**%	52.9%	**56.0**%	1.6%	**1.7**%
3-5	10.8%	**37.5**%	0.8%	**2.0**%	13.7%	**18.1**%	1.9%	**2.5**%

Table 5.7: Table of the ITS-MFT misalignment systematic uncertainties in the low mass region for the offset and weighted offset distributions, without any distortion applied to the background. In each case, the largest uncertainty is in bold. A hyphen indicates that uncertainty could not be quantified. The uncertainties obtained here are smaller and are available in more cases.

The ITS-MFT misalignment systematic uncertainties obtained without distorting the background in the low mass region are smaller in all cases. We have results for all $p_T^{\mu\mu}$ ranges for the charm and almost all of them for the beauty. Moreover, the charm systematic uncertainties have dropped considerably, down to 2.5% at maximum. We concluded that, in the low mass region, the background is so large that it avoids measuring both open beauty and open charm via dimuons in most cases.

The global MFT performance for open heavy flavor measurements via dimuons

In the end, the open beauty via dimuons will not be accessible in the low mass region, only open charm will be measurable, in the $p_T^{\mu\mu}$ range 3 to 5 GeV/c, using the offset distributions, and with a total uncertainty of ∼8.8%.

In the high mass region, both open beauty and open charm will be accessible via dimuons, in the $p_T^{\mu\mu}$ range 0 to 5 GeV/c, with the weighted offset distributions and with total uncertainties of ∼24.6% and ∼19.9% respectively.

6 Conclusions and outlook

We evaluated the performances of the Muon Forward Tracker, a future upgrade of the ALICE experiment scheduled for the run III of the LHC, for the open beauty and open charm measurements, via dimuons. For this reason, we studied the offset and weighted offset distributions, as these observables can be used to distinguish open charm and open beauty.

We started with a Monte-Carlo simulation of 0-10% central Pb-Pb collisions generated with the expected conditions of run III of the ALICE experiment: a center-of-mass energy of $\sqrt{s_{NN}} = 5.5$ TeV, and equipped with the upgraded Inner Tracking System and the Muon Forward Tracker. We divided our study in two invariant mass regions and several dimuon p_T ranges.

After applying track selections at the single muon and dimuon levels, in order to reduce the background proportion, we first built the reference beauty, charm and background offset and weighted offset templates, for both mass regions and all $p_T^{\mu\mu}$ ranges. Then we evaluated the associated systematic uncertainties by deforming the reference templates using biased configurations that depend on the source of the systematic uncertainty: by shifting the transverse plane coordinates of the primary vertex for the ITS-MFT misalignment systematic uncertainty; by smearing the single muon track coordinates in the transverse plane for the MFT pointing accuracy systematic uncertainty; and by applying weights that depend on alternative models that incorporate different energy loss mechanisms for the Monte-Carlo inputs systematic uncertainty.

We found out that, in the low mass region (from 1.2 to 2.8 GeV/c^2), only the charm component would be accessible, with the offset distributions, in the $p_T^{\mu\mu}$ range 3 to 5 GeV/c, and with a total uncertainty of 8.8% (combining statistical errors and systematic uncertainties). In the high mass region (from 4 to 9 GeV/c^2), both open beauty and open charm can be accessed, in the $p_T^{\mu\mu}$ range 0 to 5 GeV/c and with the weighted offset distributions. The total uncertainties are: 24.6% for the beauty and 19.9% for the charm.

Another observable can be used to disentangle open charm and open beauty via dimuons: the invariant mass distributions. In the present report we only built the reference templates, so a future work would be the evaluation of the associated uncertainties. This way, the invariant mass distributions could also be used to separate open charm and open beauty via dimuons.

Bibliography

[1] Francis Halzen and Alan D. Martin. *Quarks and leptons: An Introductory Course in Modern Particle Physics*. Wiley; 1st edition (January 20, 1984), 1984.

[2] J. Beringer *et al* (Particle Data Group). Review of particle physics. *Phys. Rev.*, D86:010001, 2012.

[3] Lizardo Valencia Palomo. *Inclusive J/psi production measurement in Pb-Pb collisions at* $\sqrt{s_{NN}}$ *= 2.76 TeV with the ALICE Muon Spectrometer*. Theses, Université Paris Sud - Paris XI, September 2013.

[4] Loic Manceau. *Mesure de la section efficace de production des hadrons lourds avec le spectromètre à muons d'ALICE au LHC*. PhD thesis, 2010. Thèse de doctorat dirigée par Crochet, Philippe Physique Corpusculaire Clermont-Ferrand 2 2010.

[5] X. Zhang. *Study of Heavy Flavours from Muons Measured with the ALICE Detector in Proton-Proton and Heavy-Ion Collisions at the CERN-LHC*. Theses, Université Blaise Pascal - Clermont-Ferrand II, May 2012. N° d'ordre: DU 2240 EDSF : 714.

[6] The ALICE Collaboration. The alice experiment at the cern lhc. *Journal of Instrumentation*, 3(08):S08002, 2008.

[7] B Abelev et al and The ALICE Collaboration. Technical design report for the upgrade of the alice inner tracking system. *Journal of Physics G: Nuclear and Particle Physics*, 41(8):087002, 2014.

[8] Technical Design Report for the Muon Forward Tracker. Technical Report CERN-LHCC-2015-001. ALICE-TDR-018, CERN, Geneva, Jan 2015.

[9] Addendum of the Letter Of Intent for the Upgrade of the ALICE Experiment : The Muon Forward Tracker. Technical Report CERN-LHCC-2013-014. LHCC-I-022-ADD-1, CERN, Geneva, Aug 2013.

[10] Matteo Cacciari, Stefano Frixione, Nicolas Houdeau, Michelangelo L. Mangano, Paolo Nason, et al. Theoretical predictions for charm and bottom production at the LHC. *JHEP*, 1210:137, 2012.

A Appendix

Offset and weighted offset parametrizations

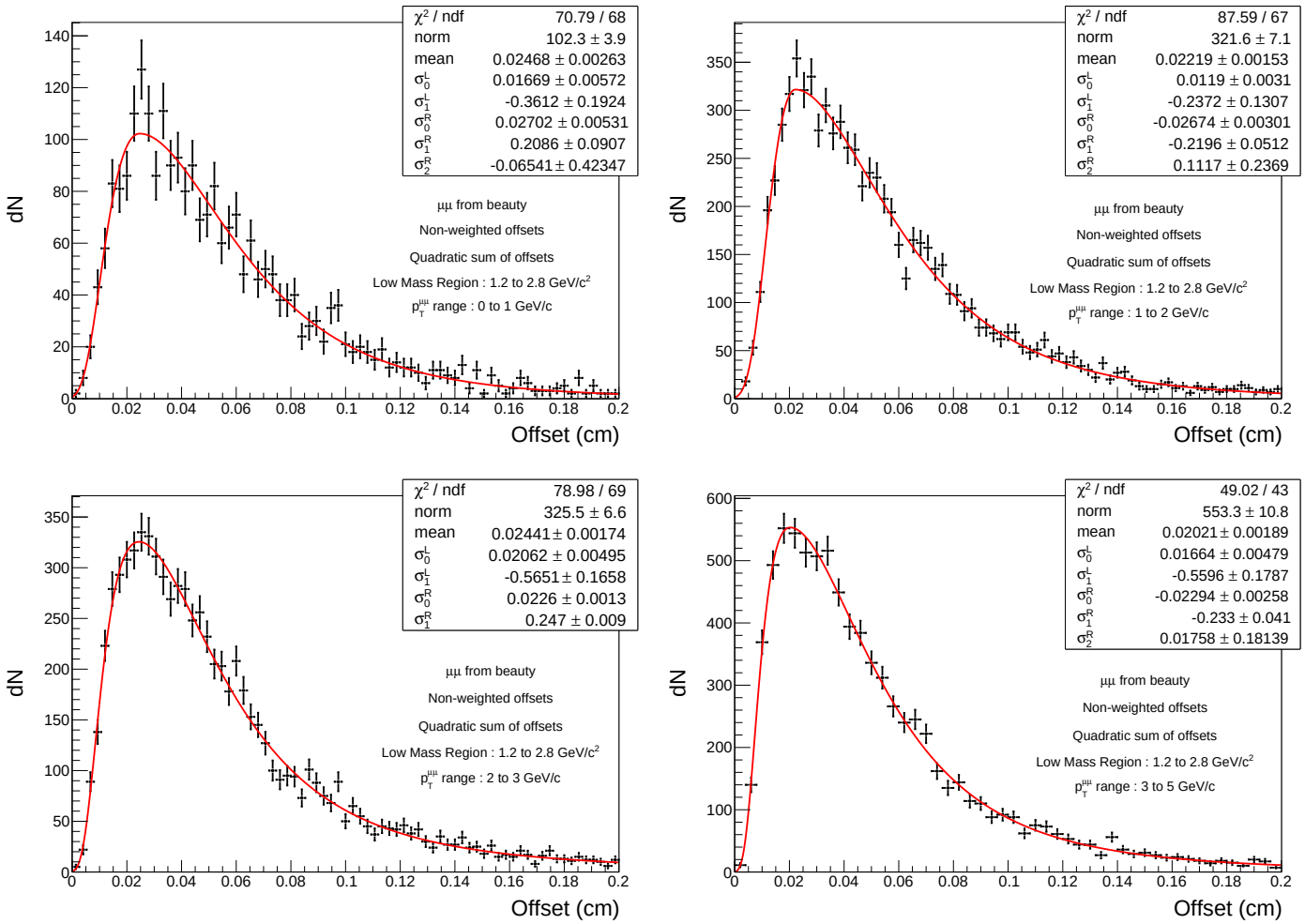

Figure A.1: Offset parametrizations for the beauty, in the low mass region, in $p_T^{\mu\mu}$ ranges: 0 to 1 GeV/c (*top left*), 1 to 2 GeV/c (*top right*), 2 to 3 GeV/c (*bottom left*) and 3 to 5 GeV/c (*bottom right*). Note that all of these offset distributions are not scaled to an integrated luminosity of 10 nb^{-1}.

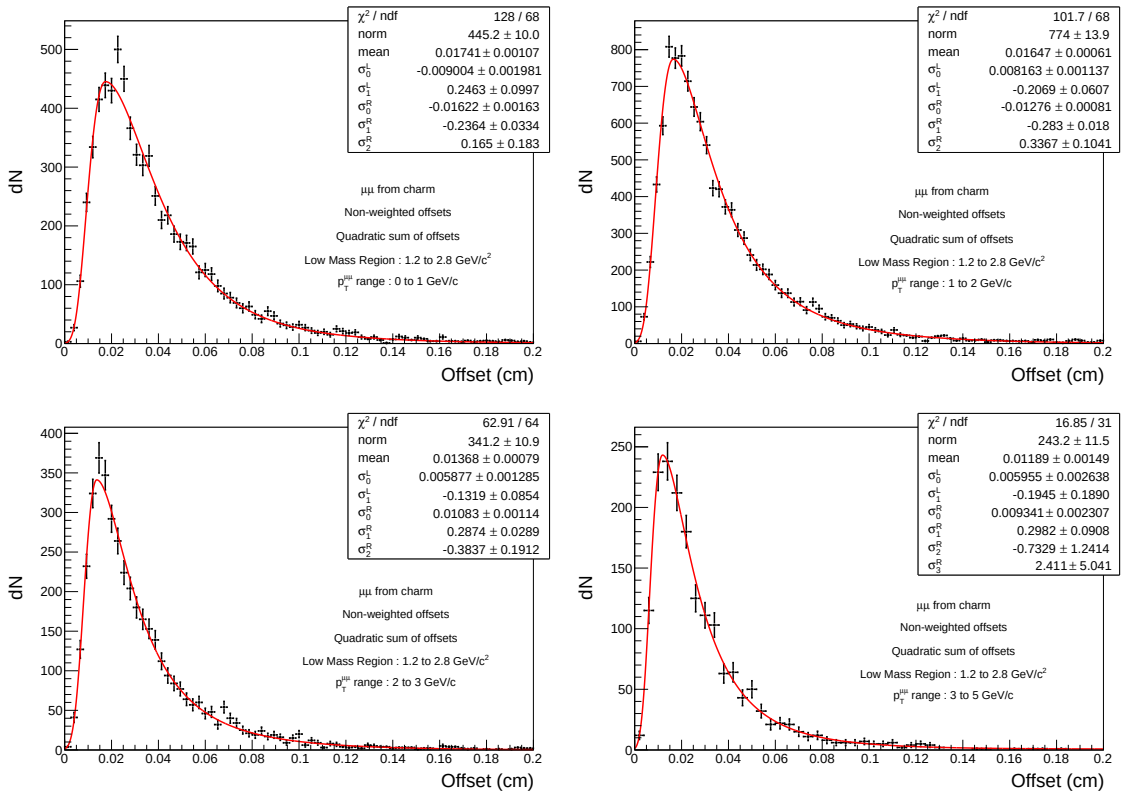

Figure A.2: Offset parametrizations for the charm, in the low mass region, in $p_T^{\mu\mu}$ ranges: 0 to 1 GeV/c (*top left*), 1 to 2 GeV/c (*top right*), 2 to 3 GeV/c (*bottom left*) and 3 to 5 GeV/c (*bottom right*). Note that all of these offset distributions are not scaled to an integrated luminosity of 10 nb^{-1}.

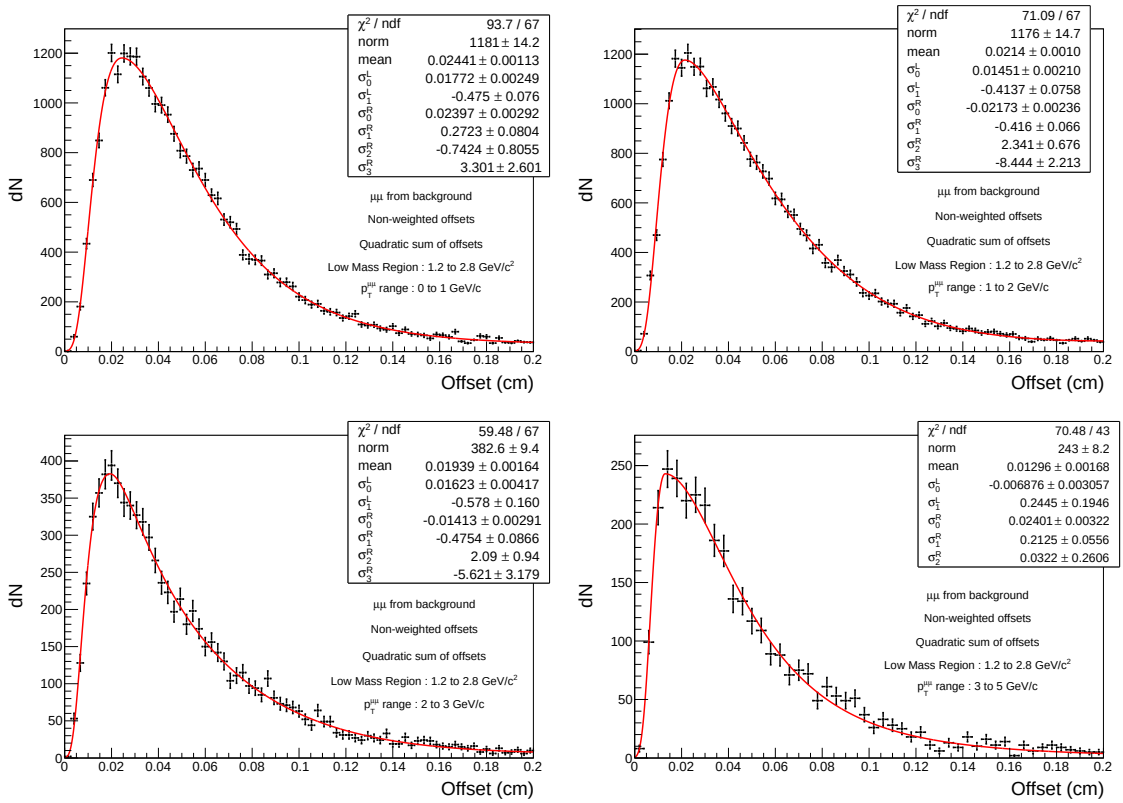

Figure A.3: Offset parametrizations for the background, in the low mass region, in $p_T^{\mu\mu}$ ranges: 0 to 1 GeV/c (*top left*), 1 to 2 GeV/c (*top right*), 2 to 3 GeV/c (*bottom left*) and 3 to 5 GeV/c (*bottom right*). Note that all of these offset distributions are not scaled to an integrated luminosity of 10 nb^{-1}.

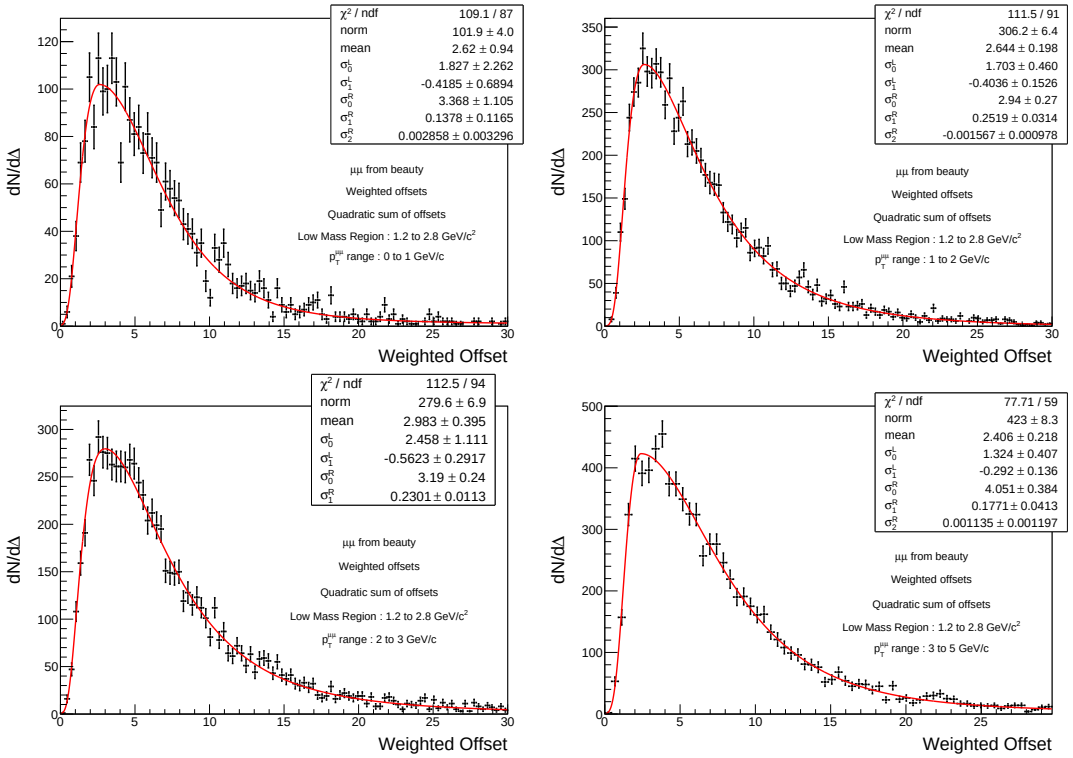

Figure A.4: Weighted offset parametrizations for the beauty, in the low mass region, in $p_T^{\mu\mu}$ ranges: 0 to 1 GeV/c (*top left*), 1 to 2 GeV/c (*top right*), 2 to 3 GeV/c (*bottom left*) and 3 to 5 GeV/c (*bottom right*). Note that all of these weighted offset distributions are not scaled to an integrated luminosity of 10 nb^{-1}.

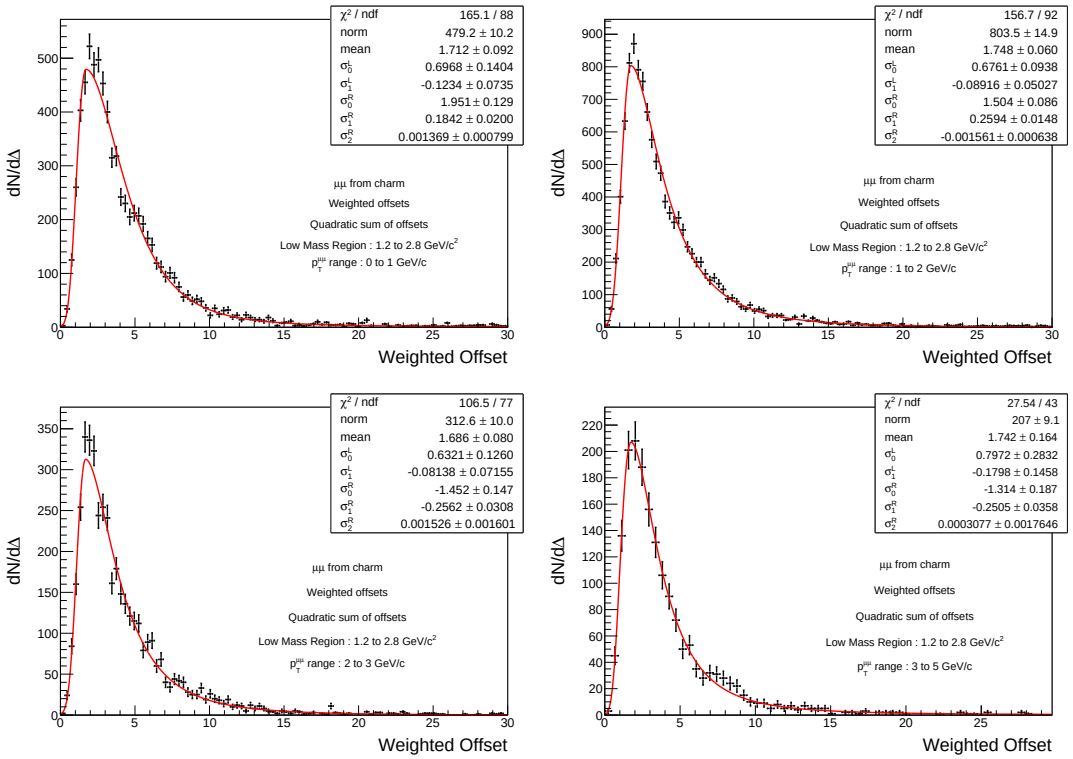

Figure A.5: Weighted offset parametrizations for the charm, in the low mass region, in $p_T^{\mu\mu}$ ranges: 0 to 1 GeV/c (*top left*), 1 to 2 GeV/c (*top right*), 2 to 3 GeV/c (*bottom left*) and 3 to 5 GeV/c (*bottom right*). Note that all of these weighted offset distributions are not scaled to an integrated luminosity of 10 nb^{-1}.

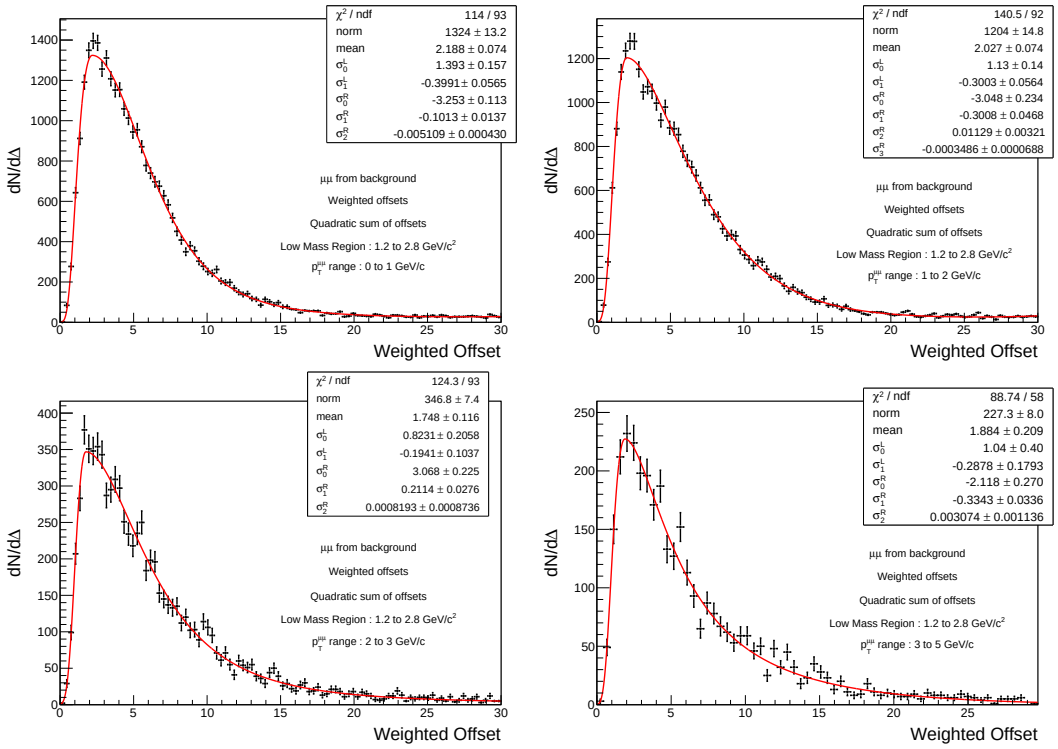

Figure A.6: Weighted offset parametrizations for the background, in the low mass region, in $p_T^{\mu\mu}$ ranges: 0 to 1 GeV/c (*top left*), 1 to 2 GeV/c (*top right*), 2 to 3 GeV/c (*bottom left*) and 3 to 5 GeV/c (*bottom right*). Note that all of these weighted offset distributions are not scaled to an integrated luminosity of 10 nb^{-1}.

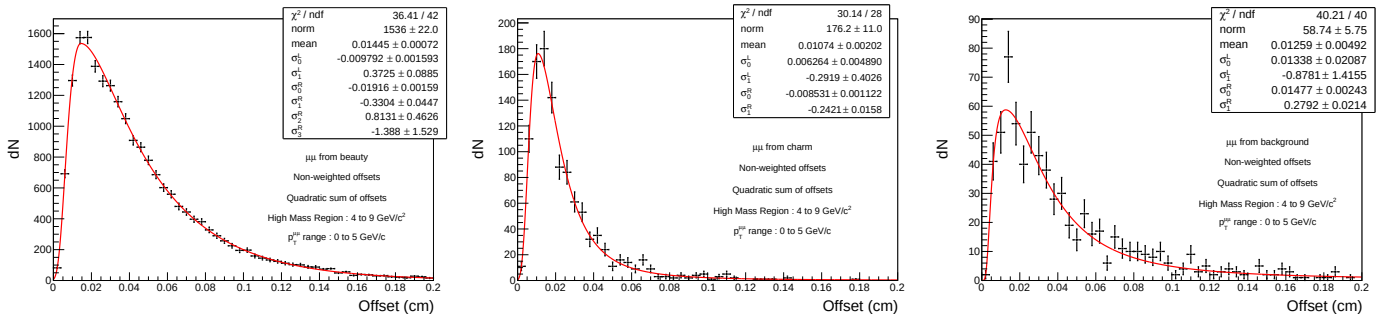

Figure A.7: Offset parametrizations in the high mass region, in $p_T^{\mu\mu}$ range 0 to 5 GeV/c, for the beauty (*left*), charm (*middle*) and background (*right*). Note that all of these offset distributions are not scaled to an integrated luminosity of 10 nb^{-1}.

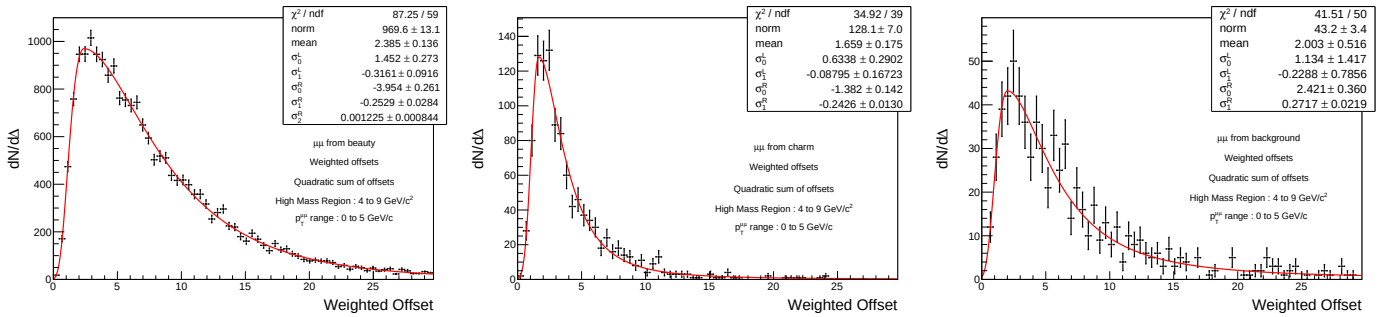

Figure A.8: Weighted offset parametrizations in the high mass region, in $p_T^{\mu\mu}$ range 0 to 5 GeV/c, for the beauty (*left*), charm (*middle*) and background (*right*). Note that all of these weighted offset distributions are not scaled to an integrated luminosity of 10 nb^{-1}.

Invariant mass parametrizations

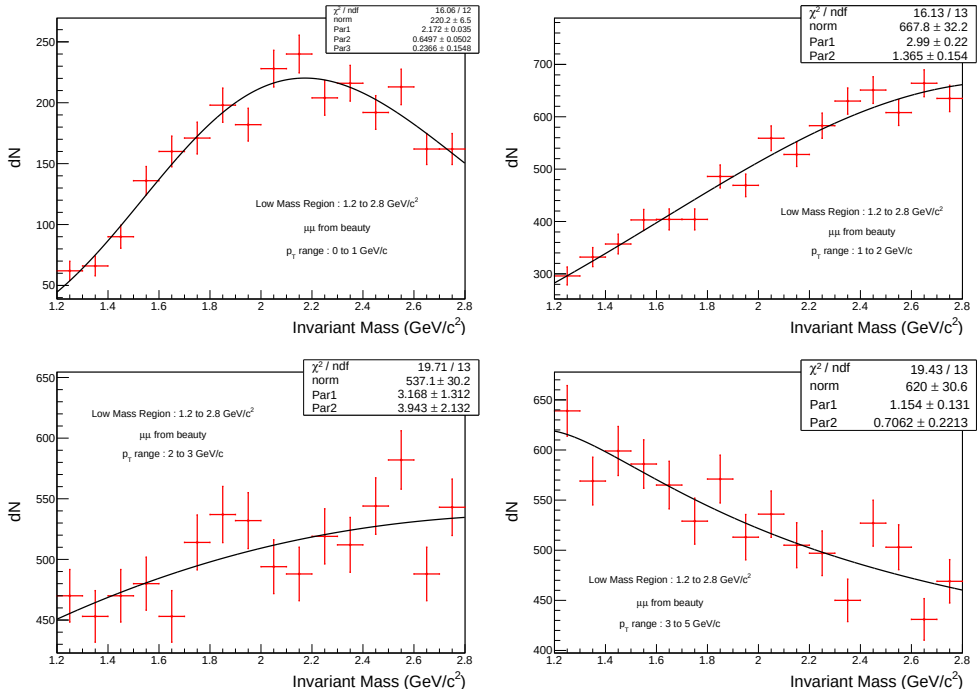

Figure A.9: Invariant mass parametrizations for the beauty, in the low mass region, in $p_T^{\mu\mu}$ ranges: 0 to 1 GeV/c (*top left*), 1 to 2 GeV/c (*top right*), 2 to 3 GeV/c (*bottom left*) and 3 to 5 GeV/c (*bottom right*). Note that all of these invariant mass distributions are not scaled to an integrated luminosity of 10 nb^{-1}.

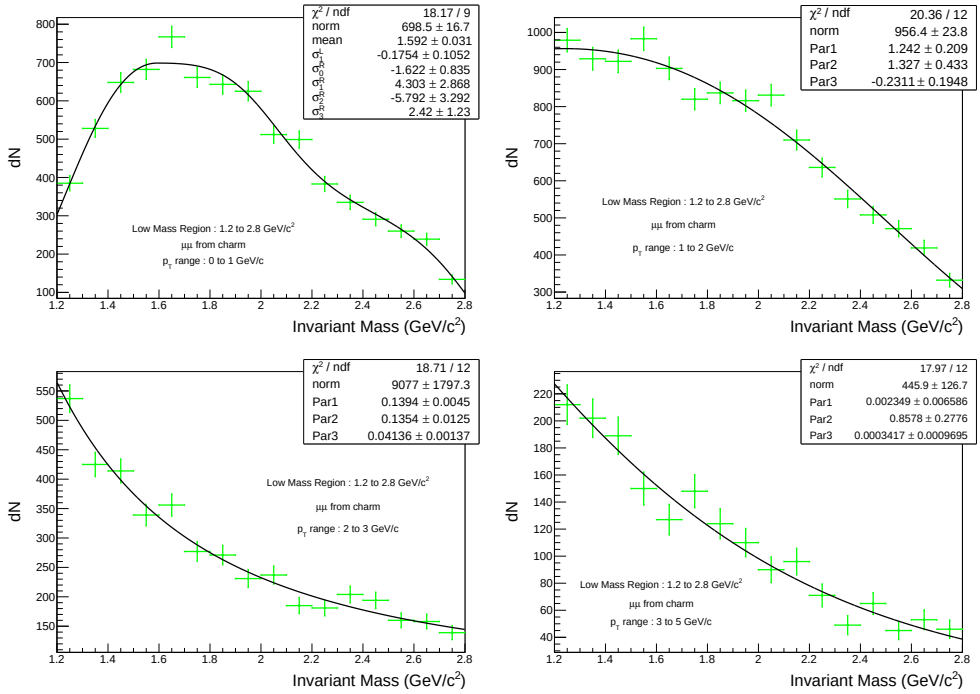

Figure A.10: Invariant mass parametrizations for the charm, in the low mass region, in $p_T^{\mu\mu}$ ranges: 0 to 1 GeV/c (*top left*), 1 to 2 GeV/c (*top right*), 2 to 3 GeV/c (*bottom left*) and 3 to 5 GeV/c (*bottom right*). Note that all of these invariant mass distributions are not scaled to an integrated luminosity of 10 nb^{-1}.

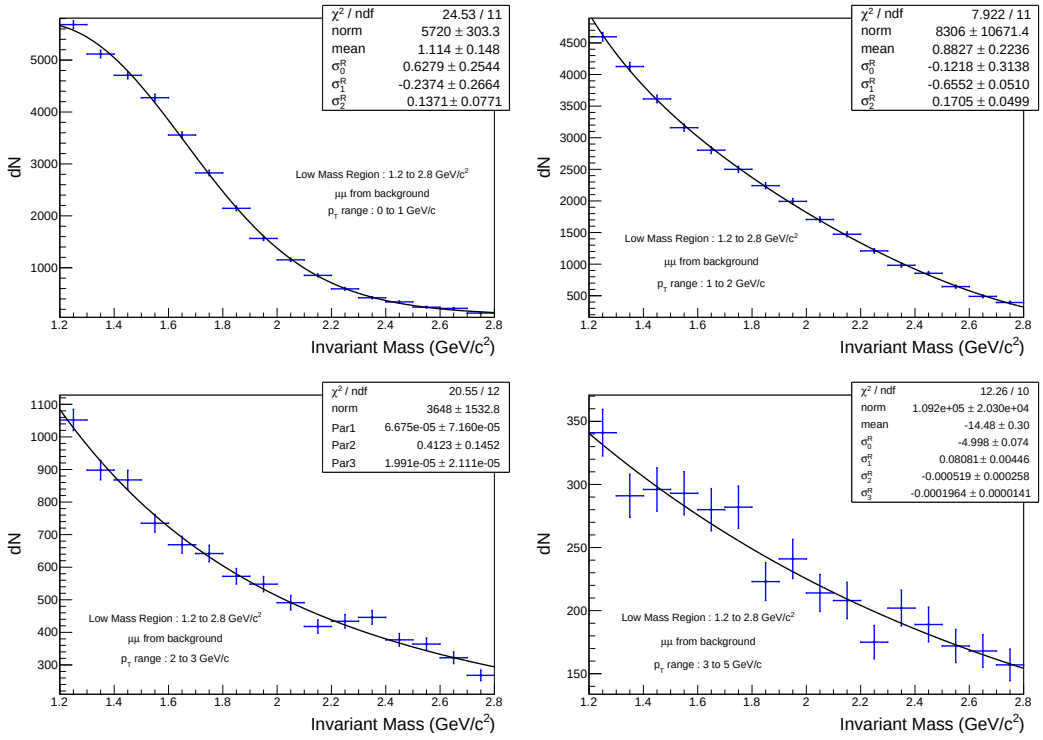

Figure A.11: Invariant mass parametrizations for the background, in the low mass region, in $p_T^{\mu\mu}$ ranges: 0 to 1 GeV/c (*top left*), 1 to 2 GeV/c (*top right*), 2 to 3 GeV/c (*bottom left*) and 3 to 5 GeV/c (*bottom right*). Note that all of these invariant mass distributions are not scaled to an integrated luminosity of 10 nb^{-1}.

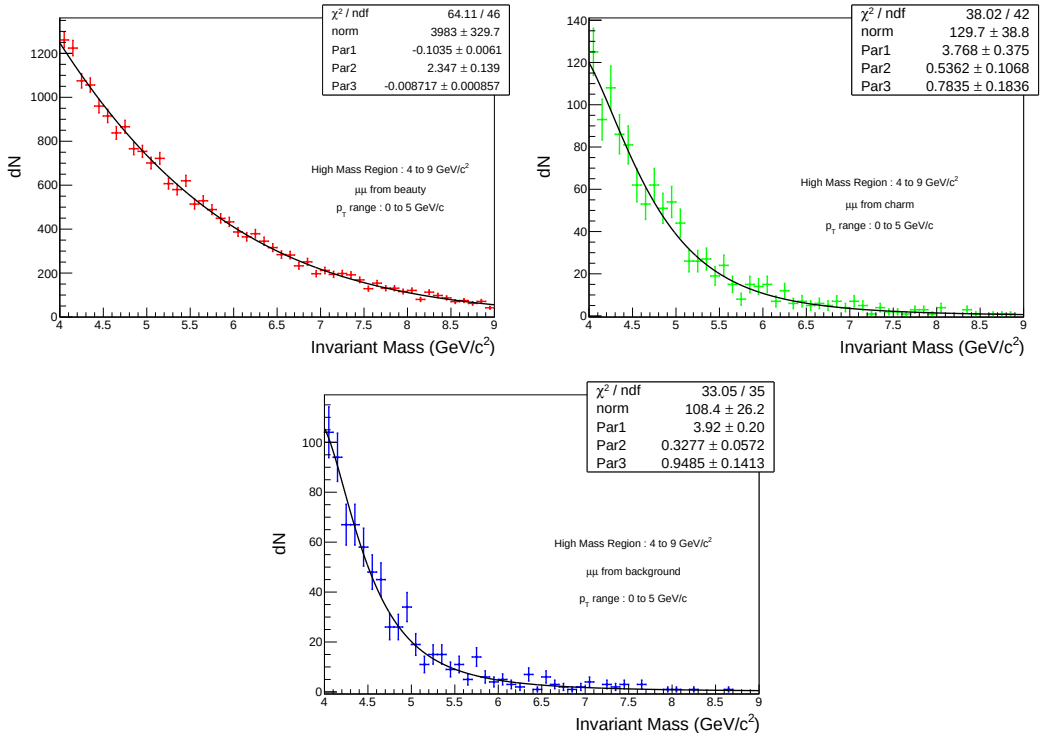

Figure A.12: Invariant mass parametrizations in the high mass region, in $p_T^{\mu\mu}$ range 0 to 5 GeV/c, for the beauty (*top left*), charm (*top right*) and background (*bottom*). Note that all of these invariant mass distributions are not scaled to an integrated luminosity of 10 nb^{-1}.

Monte-Carlo inputs: R_{AA} plots for the alternative models

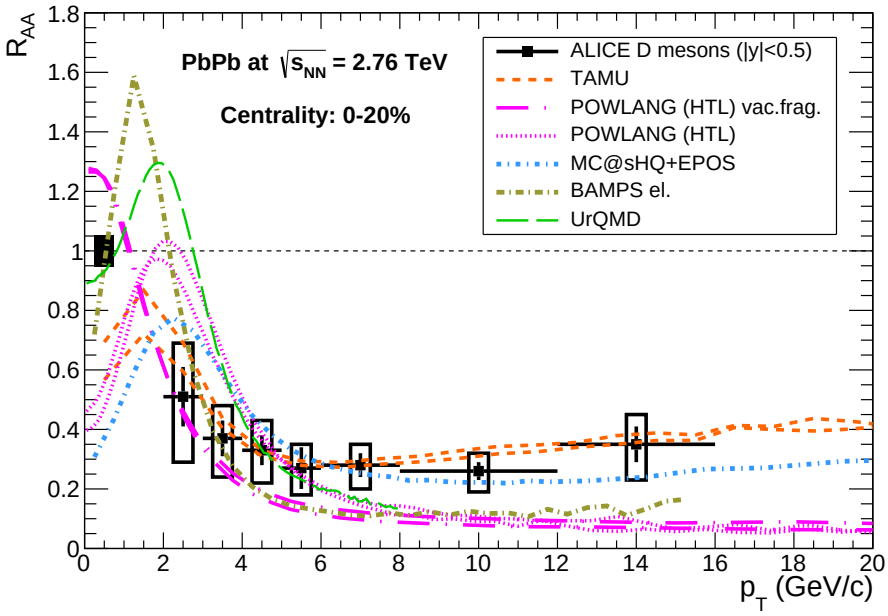

Figure A.13: R_{AA} distributions for the alternative models used for the Monte-Carlo inputs systematic uncertainties for the charm. The models include collisional energy loss.

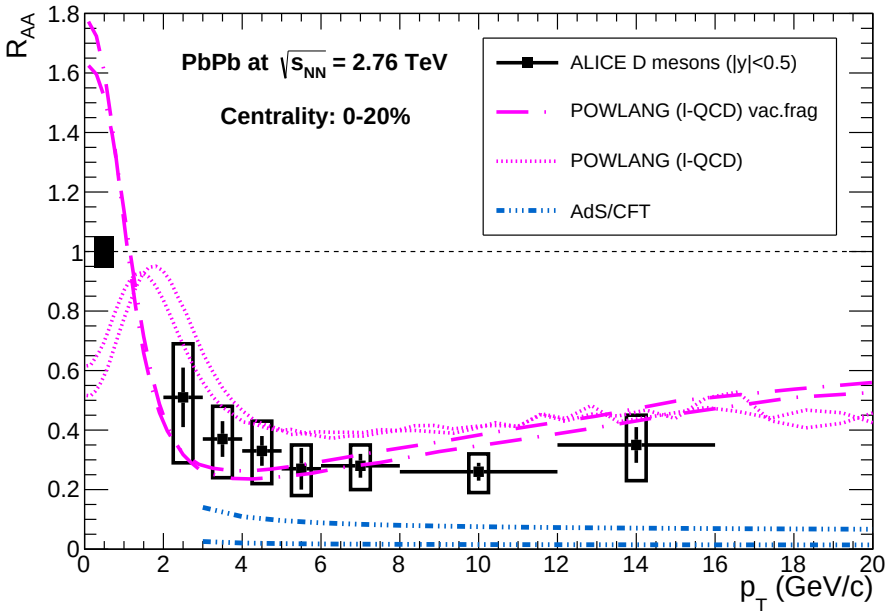

Figure A.14: R_{AA} distributions for the alternative models used for the Monte-Carlo inputs systematic uncertainties for the charm. The models include radiative energy loss.

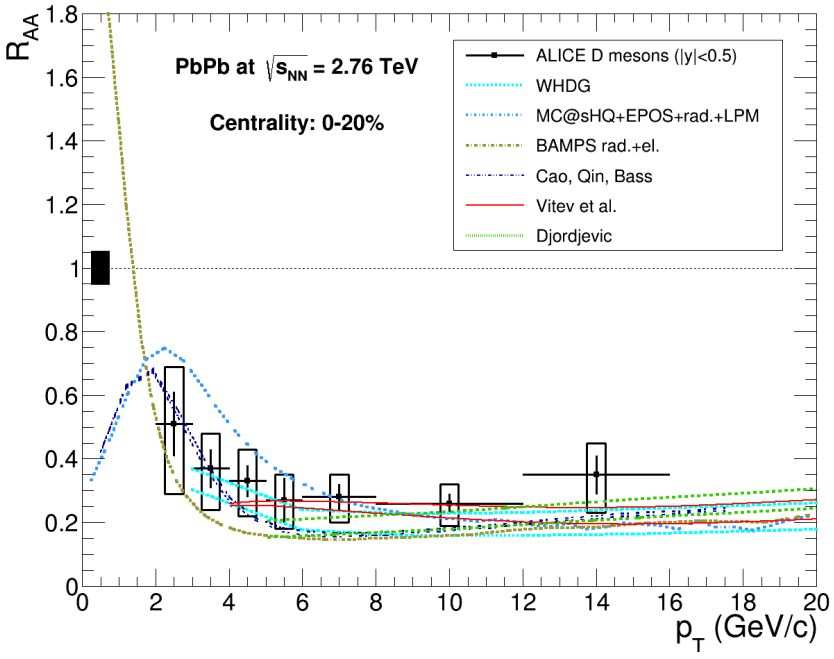

Figure A.15: R_{AA} distributions for the alternative models used for the Monte-Carlo inputs systematic uncertainties for the charm. The models include collisional and radiative energy loss.

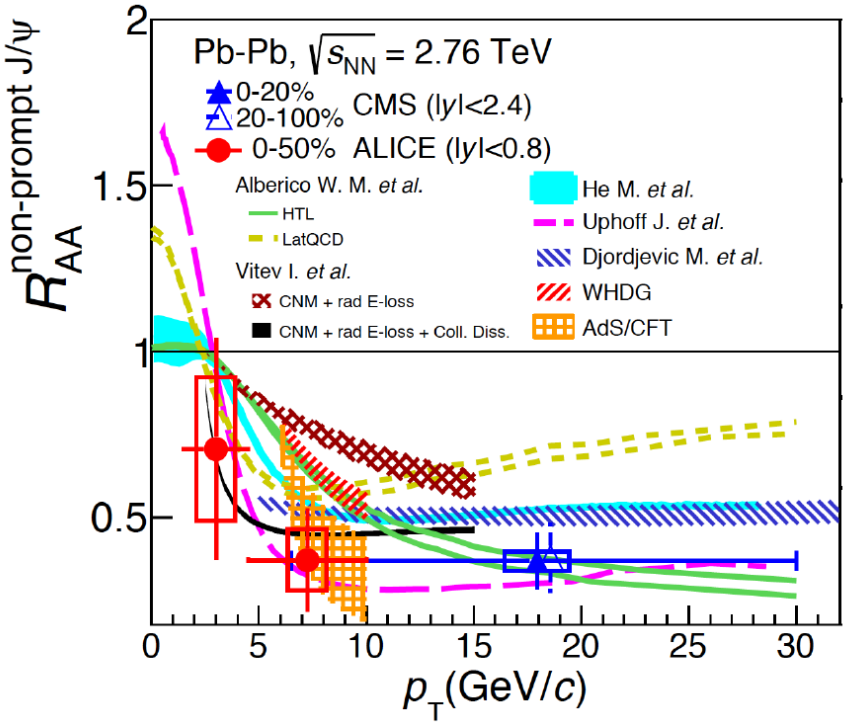

Figure A.16: R_{AA} distributions for the alternative models used for the Monte-Carlo inputs systematic uncertainties for the beauty. Models include radiative/collisional/radiative and collisional energy loss.

Distortion parametrizations for the systematic uncertainties

ITS-MFT misalignment

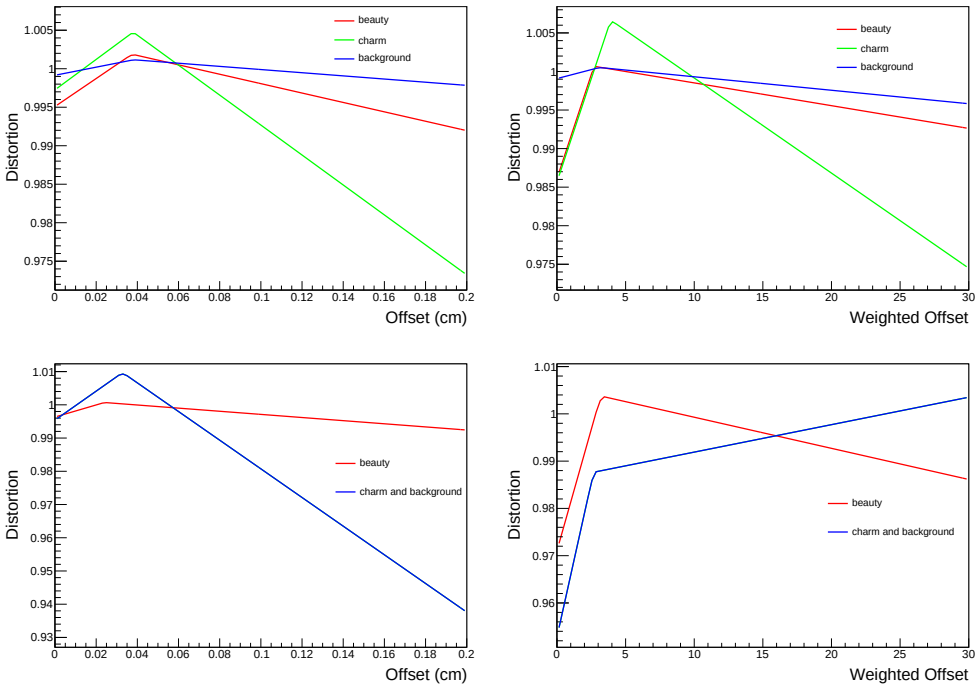

Figure A.17: Distortions for the ITS-MFT misalignment, for a + 10 μm misalignment systematic uncertainties, in the $p_T^{\mu\mu}$ range 0 to 5 GeV/c, for the low mass region: for the offset (*top left*) and weighted offset (*top right*); for the high mass region: for the offset (*bottom left*) and weighted offset (*bottom right*).

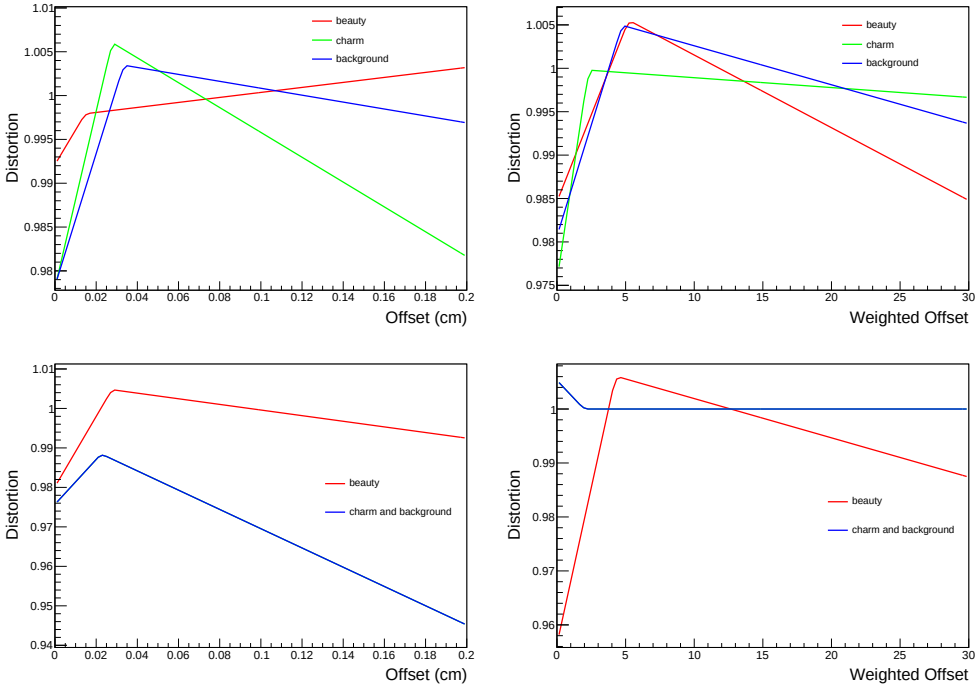

Figure A.18: Distortions for the ITS-MFT misalignment, for a - 10 μm misalignment systematic uncertainties, in the $p_T^{\mu\mu}$ range 0 to 5 GeV/c, for the low mass region: for the offset (*top left*) and weighted offset (*top right*); for the high mass region: for the offset (*bottom left*) and weighted offset (*bottom right*).

MFT pointing accuracy

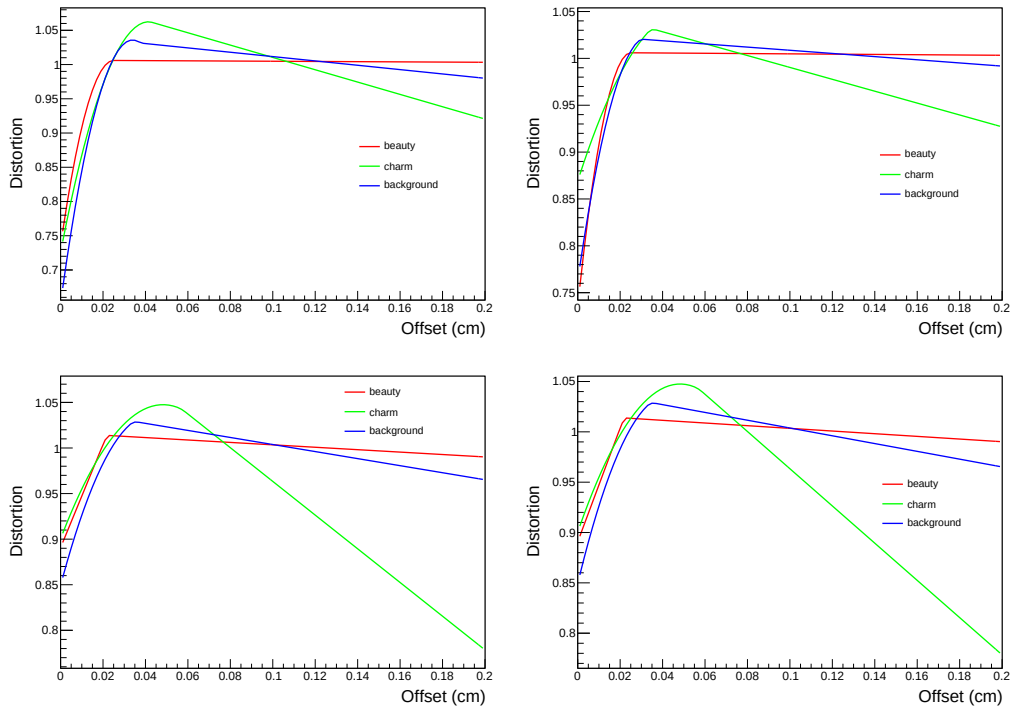

Figure A.19: Distortions for the MFT pointing accuracy systematic uncertainties in the low mass region, for the offset, in $p_T^{\mu\mu}$ ranges: 0 to 1 GeV/c (*top left*), 1 to 2 GeV/c (*top right*), 2 to 3 GeV/c (*bottom left*) and 3 to 5 GeV/c (*bottom right*).

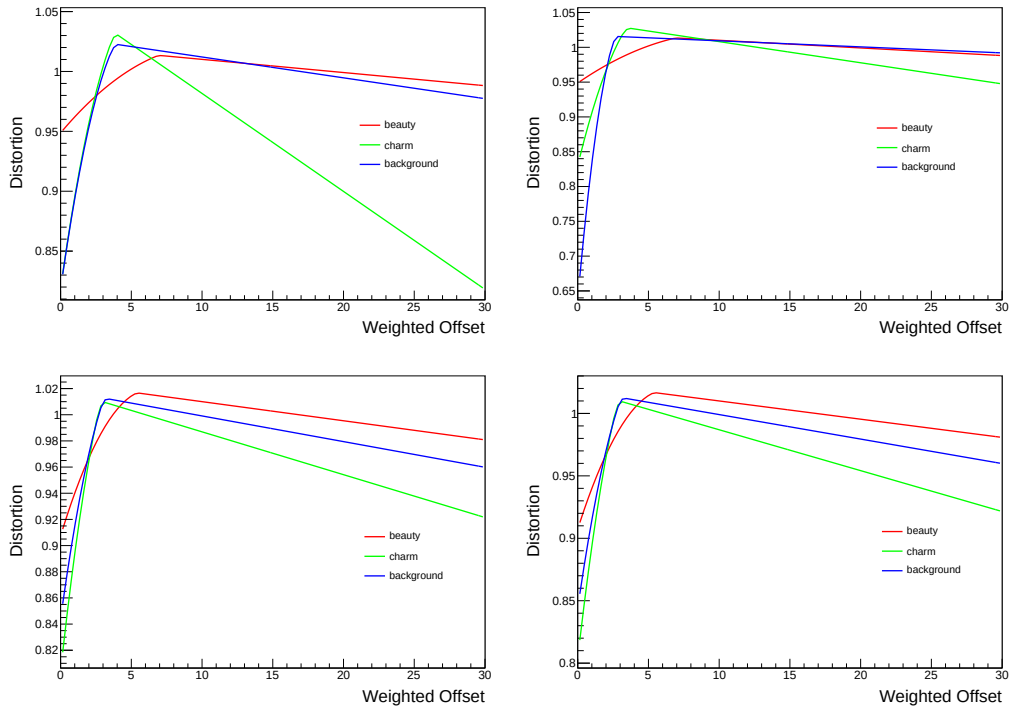

Figure A.20: Distortions for the MFT pointing accuracy systematic uncertainties in the low mass region, for the weighted offset, in $p_T^{\mu\mu}$ ranges: 0 to 1 GeV/c (*top left*), 1 to 2 GeV/c (*top right*), 2 to 3 GeV/c (*bottom left*) and 3 to 5 GeV/c (*bottom right*).

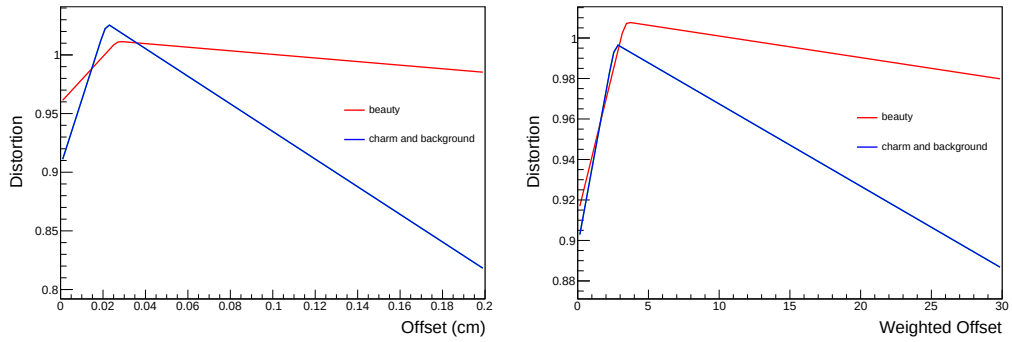

Figure A.21: Distortions for the MFT pointing accuracy systematic uncertainties in the high mass region, in the $p_T^{\mu\mu}$ range 0 to 5 GeV/c, for the offset (*bottom left*) and weighted offset (*bottom right*).

Monte-Carlo inputs

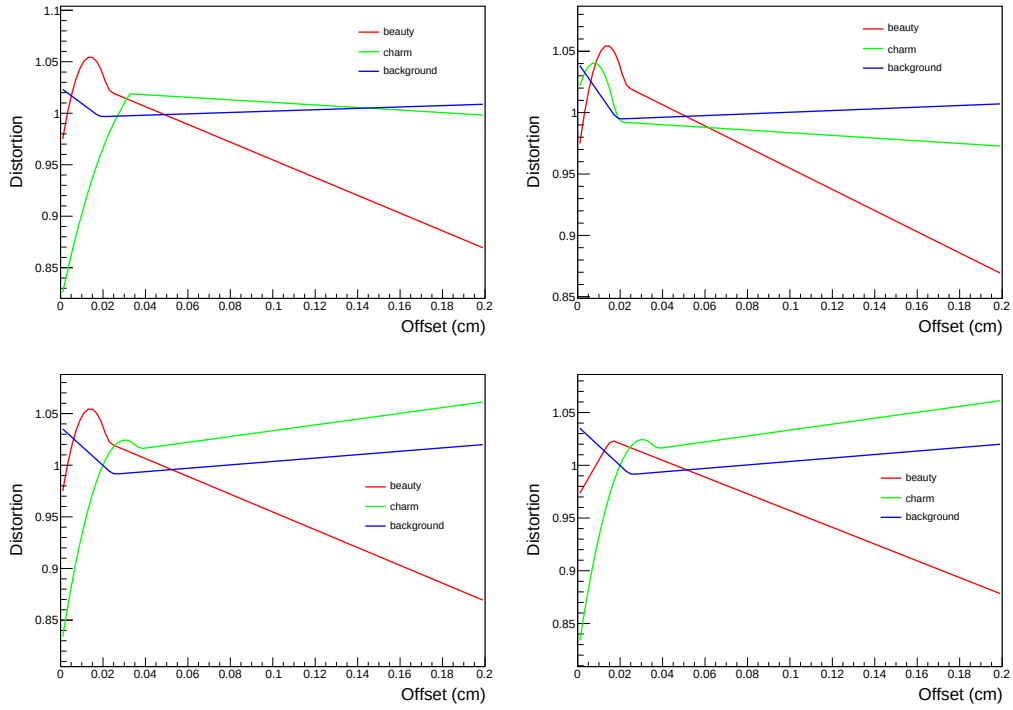

Figure A.22: Distortions for the Monte-Carlo inputs systematic uncertainties in the low mass region, for the offset, in $p_T^{\mu\mu}$ ranges: 0 to 1 GeV/c (*top left*), 1 to 2 GeV/c (*top right*), 2 to 3 GeV/c (*bottom left*) and 3 to 5 GeV/c (*bottom right*).

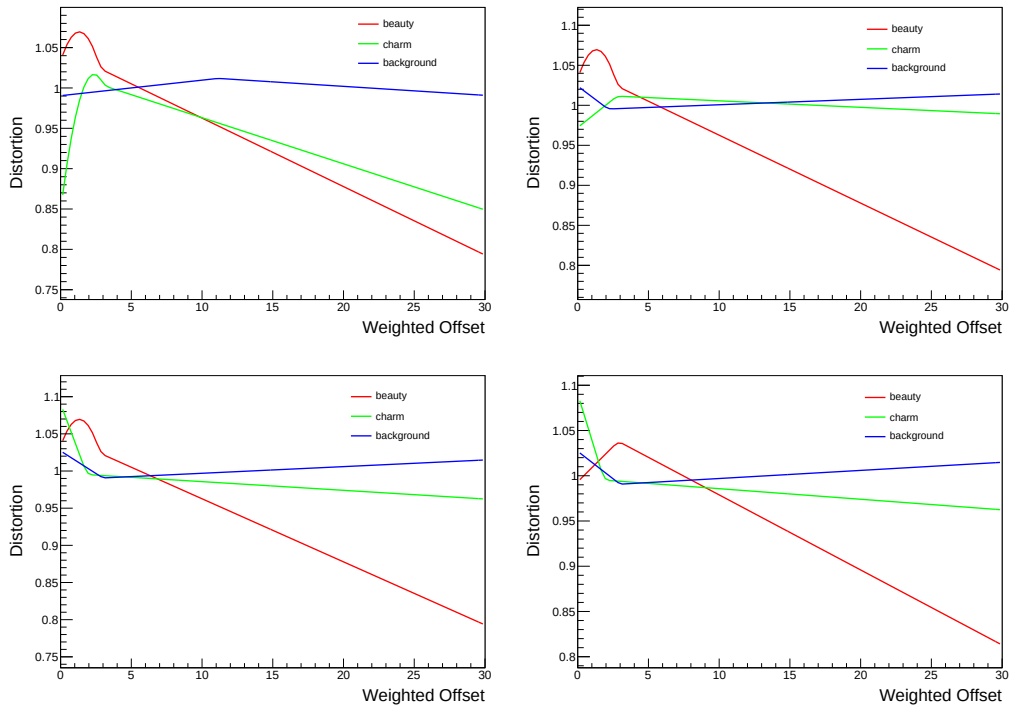

Figure A.23: Distortions for the Monte-Carlo inputs systematic uncertainties in the low mass region, for the weighted offset, in $p_T^{\mu\mu}$ ranges: 0 to 1 GeV/c (*top left*), 1 to 2 GeV/c (*top right*), 2 to 3 GeV/c (*bottom left*) and 3 to 5 GeV/c (*bottom right*).

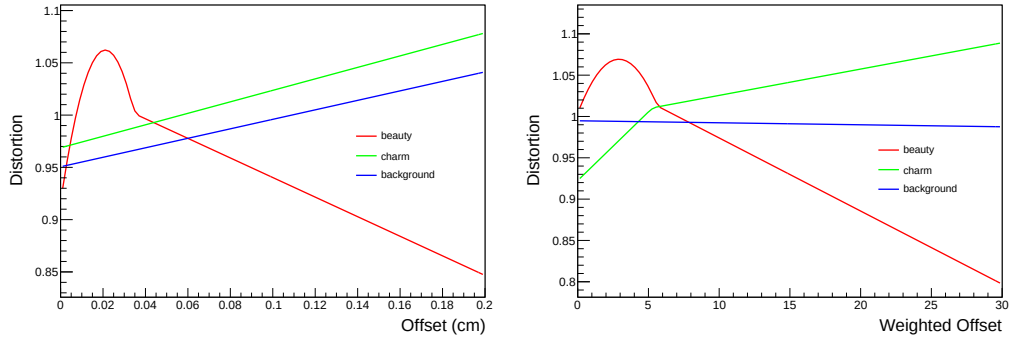

Figure A.24: Distortions for the Monte-Carlo inputs systematic uncertainties in the high mass region, in the $p_T^{\mu\mu}$ range 0 to 5 GeV/c, for the offset (*bottom left*) and weighted offset (*bottom right*).

Abstract

The ALICE (A Large Ion Collider Experiment) experiment is one the four main experiments at the LHC (Large Hadron Collider), and it has been designed to study high energy heavy ion collisions. The heavy ion collisions recreate, in the laboratory, a state of matter called the Quark Gluon Plasma (QGP), where quarks and gluons are deconfined. Due to its extremely short life-time, the QGP can not be studied directly. In this sense, heavy quarks are of particular interest as they are produced in the initial hard scatterings of the collisions so they experience the complete evolution of the system. We will study the open charm and open beauty hadrons through their semimuonic (μ) decay channels, detected by the ALICE muon spectrometer. A current muon spectrometer's setup limitation is the impossibility to distinguish beauty and charm open heavy flavors through their semimuonic decays. One of the ALICE upgrades scheduled for the run III of the LHC (that will start in 2019) is the Muon Forward Tracker (MFT). This detector will be used in conjunction with the muon spectrometer at forward rapidities and the upgraded Inner Tracking System detectors, in the central barrel, and should improve several measurements. In particular, it will allow to disentangle muons from open charm and open beauty. Such a distinction would allow us to verify several theoretical predictions, and moreover, it will give us more insight on the QGP. In this study, we evaluate the future MFT perfomances in Pb-Pb collisions for the open charm and open beauty measurements, using the offset distributions, via dimuons. We started from a Monte-Carlo simulation with the expected conditions of run III of the ALICE experiment. We extracted the dimuon offset distributions, and evaluated the uncertainties for the open beauty and open charm extraction, in two invariant mass regions and several dimuon transverse momentum ($p_T^{\mu\mu}$) ranges.

Résumé

L'expérience ALICE (A Large Ion Collider Experiment) est l'une des quatres principales expériences au sein du LHC (Large Hadron Collider), et a été crée pour l'étude des collisions d'ions lourds. Les collisions d'ions lourds permettent de recréer en laboratoire un état de la matière appelé Quark Gluon Plasma (QGP), où quarks et gluons sont déconfinés. En raison de la durée de vie extrêmement courte du QGP, nous ne pouvons l'étudier directement. En ce sens, les quarks lourds sont d'un intérêt particulier car ils sont produits au cours des processus durs, au début de la collision, et donc interagissent avec le QGP tout au long de son évolution. Nous étudions les hadrons charmés et beaux à travers leurs canaux de désintegrations semi-muoniques (μ), détectés par le spectromètre à muon d'ALICE. Une des limitations actuelles du spectromètre à muon est l'impossibilité de séparer les muons provenant des saveurs lourdes charmées et belles. L'un des upgrades d'ALICE prévus pour le run III du LHC (qui débutera en 2019) est le Muon Forward Tracker (MFT). Ce détecteur sera utilisé en conjonction avec le spectromètre à muon et les futures détecteurs de l'Inner Tracking System, dans le tonneau central, et permettra d'améliorer plusieurs mesures. En particulier, il rendra possible la séparation des saveurs lourdes charmées et belles, via leur canaux de désintégration semi-muoniques. Une telle séparation permetterait de vérifier plusieurs prédicitions théoriques, et plus généralement, cela nous donnerais plus de détails sur le QGP. Dans cette étude, nous évaluons les futures performances du MFT en collisions Pb-Pb pour la mesure des saveurs lourdes charmées et belles, en utilisant les distributions d'offset, en dimuon. Nous partons d'une simulation Monte-Carlo réalisée dans des conditions similaires à celles prévues pour le run III d'ALICE. Nous en extrayons les distributions d'offset en dimuon, et évaluons les incertitudes associées à l'extraction des saveurs lourdes charmées et belles, dans deux régions en masse invariantes et plusieurs intervalles en impulsion transverses dimuoniques ($p_T^{\mu\mu}$).